FERMILAB-Proposal-0672

January, 1981

Scientific Spokesperson: A. Dzierba
Indiana University
Bloomington, IN 47405
FTS: 331-6905, 331-6907
Commercial: (812) 337-9421

Deputy Spokesperson: C. Halliwell
University of Illinois at Chicago
Chicago, IL
(312) 996-3407

A STUDY OF HADRONIC FINAL STATES PRODUCED IN ASSOCIATION WITH HIGH-P_t JETS AND HIGH-MASS DIMUONS

H. Haggerty, E. Malamud, P. Rapp

Fermi National Accelerator Lab
Batavia, IL

J. Albright, R. Diamond, J. H. Goldman, S. Hagopian, V. Hagopian, J. Lannutti

Florida State University
Tallahassee, FL

R. Ellsworth

George Mason University
Fairfax, VA

R. Abrams, H. Goldberg, C. Halliwell, S. Margulies, D. McLeod, J. Solomon

University of Illinois at Chicago Circle
Chicago, IL

B. Brabson, R. Crittenden, A. Dzierba, J. Florian, R. Heinz, J. Krider

T. Marshall, J. Martin, D. Petersen, P. Smith, S. Teige

Indiana University
Bloomington, IN

J. Goodman, R. G. Glasser, G. B. Yodh

University of Maryland
College Park, MD

T. Watts

Rutgers University
New Brunswick, NJ

96 pgs.

Abstract

We are proposing to make a systematic study of parton-parton scattering in hadron-hadron reactions initiated by 500 GeV/c mesons and protons and 1 TeV/c protons. Parton-parton subprocesses which yield high-p_t jets and/or high mass dimuons will be studied. The p_t dependence of those subprocesses yielding high-p_t jets will be measured as a function of incident particle species. The p_t, x_F and mass dependence of high-mass dimuons will also be measured in an "open-geometry" configuration. A systematic study of hadrons (with particular attention to the details of the beam jet) produced in association with dimuons or high-p_t jets will be made. We propose to add a forward calorimeter and Cerenkov counter to the existing Multiparticle Spectrometer (MPS) in the M6W beamline in order to make detailed measurements of the forward going beam jet in these processes. A dimuon trigger will also be added. The existing calorimeter will be used to detect and to trigger on high-p_t jets. We are requesting 2000 hours of beam time for data taking in addition to 500 hours for setup and testing.

CONTENTS

I Physics Motivation

II Description of Experiment

III Trigger

IV Rate Calculations and Yields

V Analysis

VI Comparison With Other Experiments

VII Requests for Resources from Fermilab

Appendices

A. Beam Identification at 500 GeV/c

B. Secondary Charged Particle Identification

C. Spectrometer Resolution

D. Trigger Calorimeter: Electronics, Calibration and Monitoring

E. Dimuon Trigger and Processor

F. Forward Calorimeter

G. Chamber System for Particle Tracking

H. Monte Carlo Simulation

References

I. Physics Goals

Introduction

Over the last few years most of the hadron-hadron experiments studying parton-parton interactions have fallen into two categories: those studying reactions yielding high-mass dilepton pairs and those studying reactions yielding high-p_t "jets" of hadrons. Within the context of quantum chromodynamics (QCD) the former class of reactions are thought, at least to first order, to be described by the diagram of Figure I-1. This is the so-called "classical" Drell-Yan diagram.[1,2] The latter class of reactions are described by the diagram of Figure I-2.[3,4] These reactions are expected to show the 4-jet structure displayed in Figure I-3. Two of the jets result from the fragmentation of the beam and target remnants while the other two jets result from the fragmentation of the scattered partons. The Drell-Yan events are expected to show a 2-jet plus 2 high-p_t lepton structure, the two jets being the beam and target jets.

The two processes described above are closely related. The structure functions, which are a measure of the probability of finding a parton of a particular flavor and momentum in the beam and target hadrons, are the same for both processes. The parton-parton scattering subprocesses of Figure I-2 include quark-quark (qq), quark-gluon (qg), quark-antiquark ($q\bar{q}$) scattering while in Figure I-1 the subprocess is $q\,\bar{q}$ annihilation. As we will see from what follows, other more complicated diagrams also contribute to dimuon production giving rise to final state dimuons and jets. To date experimental techniques employed to study the Drell-Yan mechanism and jets have been, to some extent, mutually exclusive. An experiment which provides

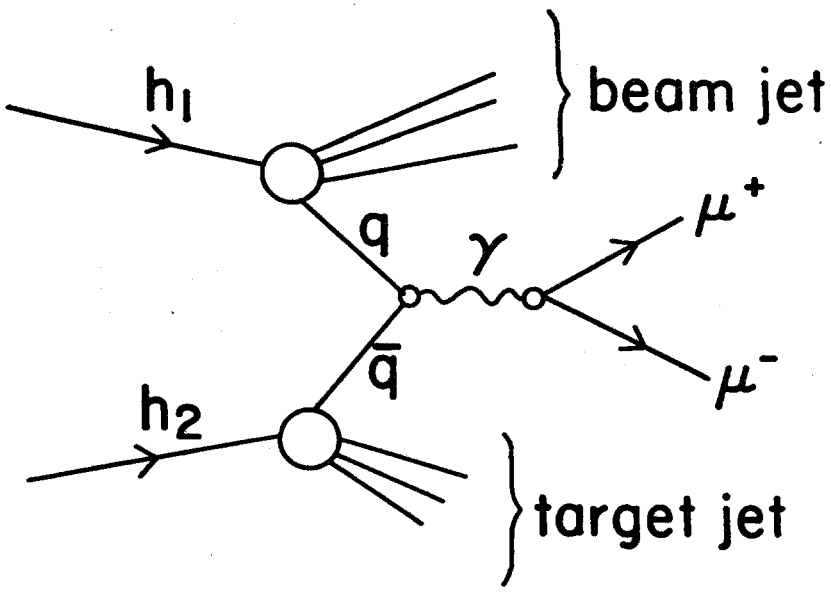

Figure I-1: Diagram describing the Drell-Yan production of high mass dimuons.

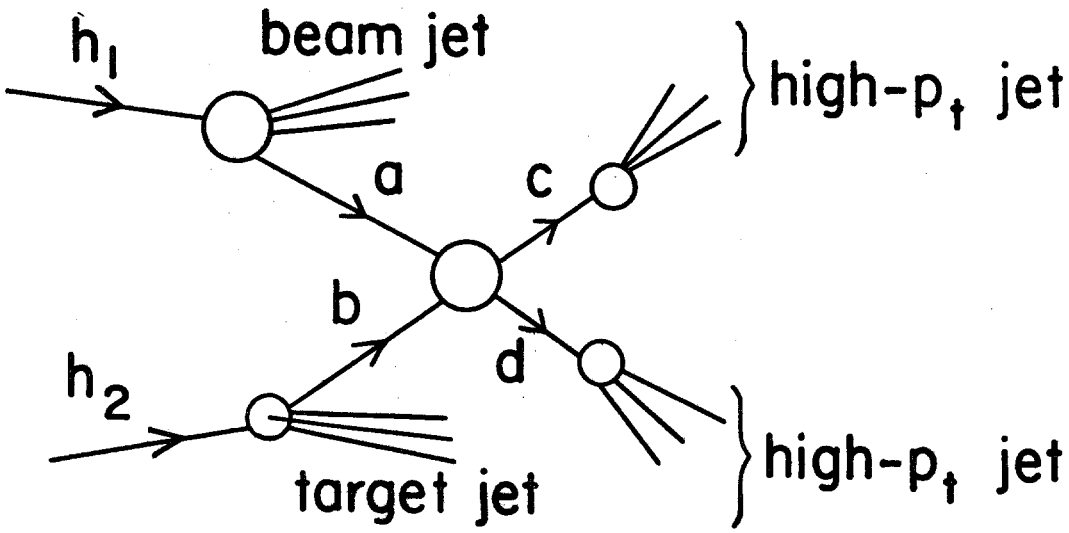

Figure I-2: Diagram describing the production of jets in hadron-hadron collisions. The subprocess involves the parton-parton scattering process $ab \rightarrow cd$. Partons c and d fragment into high-p_t jets.

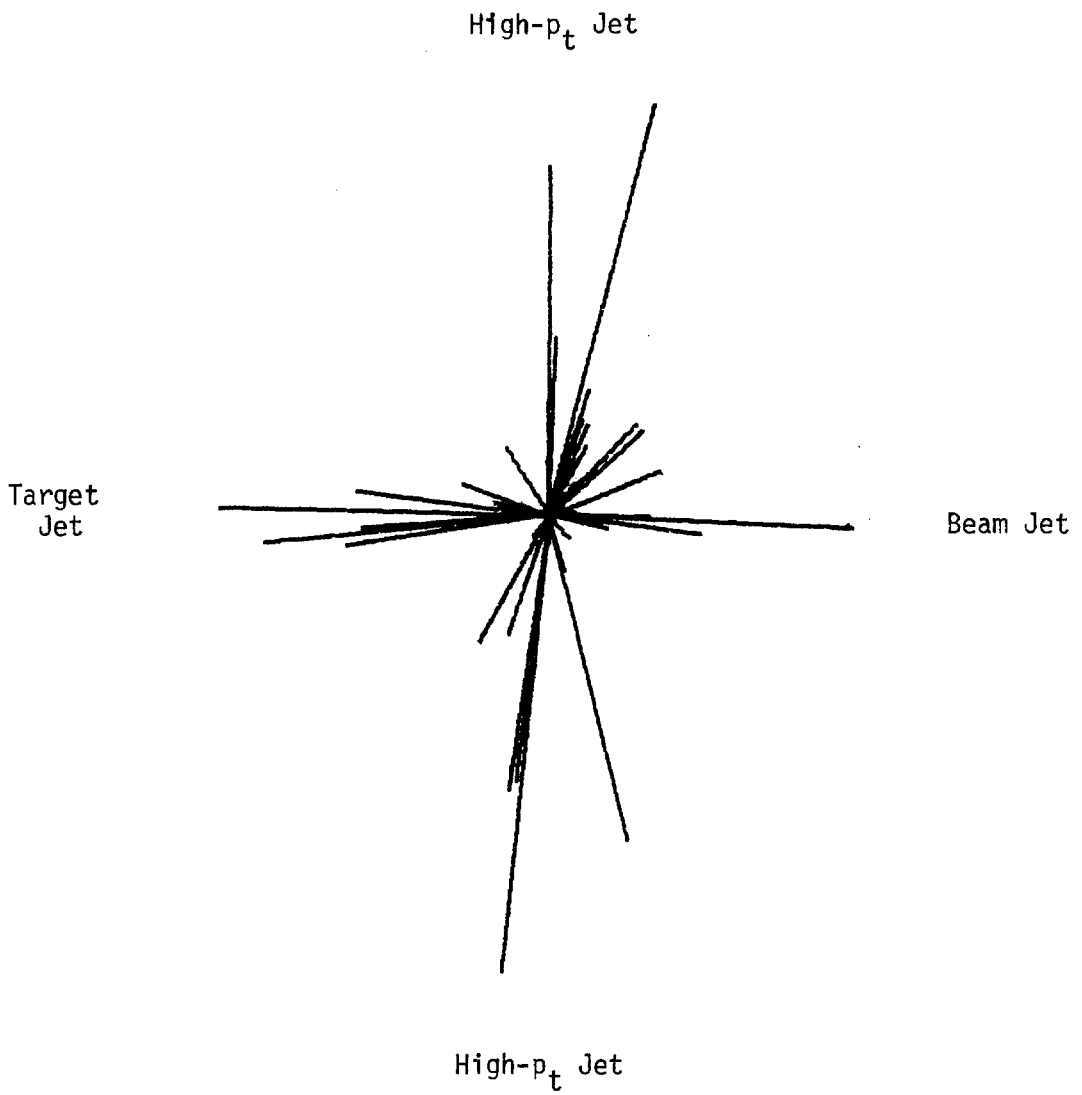

Figure I-3: Monte-Carlo simulated high-p_t jet event at p_{inc} = 800 GeV/c.
The momenta of the particles are shown in the hadron-hadron center of mass.

a trigger on high-mass dilepton pairs along with the ability to detect and/or trigger on jets will allow for a systematic study of parton-parton scattering and provide various tests of QCD.

In this section we discuss the physics questions which can be studied at Tevatron energies with regard to answering detailed questions about the subprocesses which give rise to high mass dimuons and high-p_t jets or both. In a few years the detailed theoretical framework within which we understand, or think we understand, hadron-hadron physics at the constituent parton level will undoubtedly change. Independent of theoretical details, what we are proposing is a systematic study, in a single experiment, of two phenomena in hadron-hadron interactions which surely are manifestations of parton-parton interactions. The goal of this experiment is to use the highest Tevatron energies available to study:

a. jet and dimuon production at the highest available incident hadron momenta (1 TeV/c protons and 500 GeV/c π's) in order to probe the regions of high p_t or large dimuon masses (the 500 GeV/c runs will also provide significant statistics with incident K's and $\bar{p}$'s);

b. structure of hadrons accompanying high mass dimuons (e.g. how many jets and what kind of jets accompany dimuons);

c. jet production and dimuon production in both resonance and continuum regions as a function of incident hadron species and different nuclear targets.

In what follows we first discuss the physics of high-p_t jets and then the physics of dimuon production at Tevatron energies. We also discuss the relationships between the two phenomena.

High-p_t Jets

The development of QCD and the observation and study of high-p_t hadron jets in hadron-hadron collisions[3-13] has opened the field of study of parton-parton interactions. With the arrival of the Tevatron, transverse momenta will be reached for which first-order QCD calculations for hadron-hadron interactions can be made with some confidence.[14,15] This occurs at $p_t \sim 10$ GeV/c where the running coupling constant, $\alpha(Q^2)$ becomes less than 0.2. For transverse momenta less than 10 GeV/c an empirical parameterization has been relatively successful.[16] However, within the framework of QCD there are two problems: multiple gluon emission and the applicability of perturbative QCD. These problems have already been overcome at PETRA where center-of-mass (c.m.) energies have been achieved that are high enough for QCD predictions of hard gluon emission to be checked.[17]

At Tevatron energies we expect to reach transverse momenta of ~ 14 GeV/c (equivalent to 28 GeV at PETRA), where we hope to make a variety of new QCD tests. For example, we will study the various 'Born' terms. We will also be be able to study the fragmentation of direct gluons (i.e. final state gluons which result from the subprocesses $gq \rightarrow gq$ and $gg \rightarrow gg$) as well as bremsstrahlung gluons. At PETRA the study of direct gluons is not possible. An analysis of forward going systems initiated by π and K beams (not possible at the ISR) as well as protons will also be made. (Beam particle identification is discussed in Appendix A).

The fundamental processes cannot be studied directly. Instead, the 'jets' of particles that originate from the scattered partons will be observed in our jet triggered calorimeter experiment (see Appendix D) Based on recent results from PETRA, it has been seen that scattered jets will become narrower as the energy of the scattered parton increases.[17] This is

especially important for hadron-hadron collisions where four jets (or five if one includes hard gluon bremsstrahlung) are expected in the final state. In the following paragraphs we shall discuss what we can learn about the subprocesses, the fragmentation of the jets, and the associated forward jet.

Subprocesses

The subprocesses that dominate high p_t hadron-hadron scattering are $qq \to qq$ $qg \to qg$ and $gg \to gg$. Gluons in a hadron have, on average, less momentum than quarks. Consequently, the qq scattering will dominate at high x_t ($= 2p_t/\sqrt{s}$) and qg scattering will dominate at low x_t. The cross-over point occurs at $x_t \cong 0.3$.[18] For example, when jets are produced at 90° in the parton-parton c.m. frame with $x_t \sim 0.6$, more than 90% of them will have originated from qq scattering whereas for $x_t = 0.15$ ($p_t \simeq 3$ GeV/c for $p_{inc} = 1$ TeV/c) about 75% will have originated from qg scattering.

The lower gluon momentum tends to produce jets that are not at 90° in the parton-parton c.m. frame; the gluon jet tends to be more forward going (or backward going) in the laboratory. Therefore, by applying an angular cut further separation of qg scattering can be achieved, even in the kinematical region where qq scattering is of comparable magnitude ($x_t \sim 0.3$). For example, qg scattering will be five times more probable than qq scattering for producing one parton at 60° and the other at 45° (both with $x_t = 0.3$) in the parton-parton cm frame.

In the forward direction there is a kinematical overlap between particles in the beam jet which carry a small fraction of the beam jet momentum and particles in the scattered jets which carry a small fraction of the scattered jet momentum. Monte-Carlo studies show that we will be able to determine the direction of a jet with 10 GeV/c transverse

momentum to within 5° when a polar angle cut of $\sim 15^{\circ}$ is imposed about the incident hadron direction. Jets from PETRA have secondaries with average opening angles of 17°.[17] The separation of beam jet and scattered jets observed in E260 is shown in Figure I-4.[11]

Besides separating qq and qg processes, it would be interesting to separate uu from ud scattering. This will require identifying the original partons. The leading hadron in a jet reflects the identity of the parton only 50% of the time. A technique has been suggested[19] which would allow one to identify the parton which gives rise to any particular jet. This technique improves as the number of particles in the jet increases.

In principle, it should be possible to measure the structure functions of the colliding hadrons by reconstructing the entire event. The results could then be compared to those obtained from lepton-hadron scattering experiments. In practice, the geometrical overlap between jets will cause large errors in the reconstruction of the original momentum of the parton.

Monte-Carlo simulation has shown that,on the average,for every track included incorrectly in a jet, a 6% error occurs in reconstructing the parton's momentum. Therefore we expect to reconstruct the fragmenting parton's original momentum (or alternatively, the value of Feynman x) with an accuracy in the range 10 to 20%.

Fragmentation

Experiments at PETRA[17] have accumulated a great deal of information about the non-perturbative fragmentation of quarks. It is imperative that similar information be obtained for jets produced in hadron-hadron interactions since the nature of the quarks that separate in the final state are very different from those in e^+e^- annihilation. For the latter, one has a quark-antiquark ($u\bar{u}$, $c\bar{c}$, etc.) system while in hadron-hadron collisions (pp, Kp, πp, etc.) one has either a quark-quark (uu, ud, dd, etc.), a quark-diquark (u-ud, d-uu,

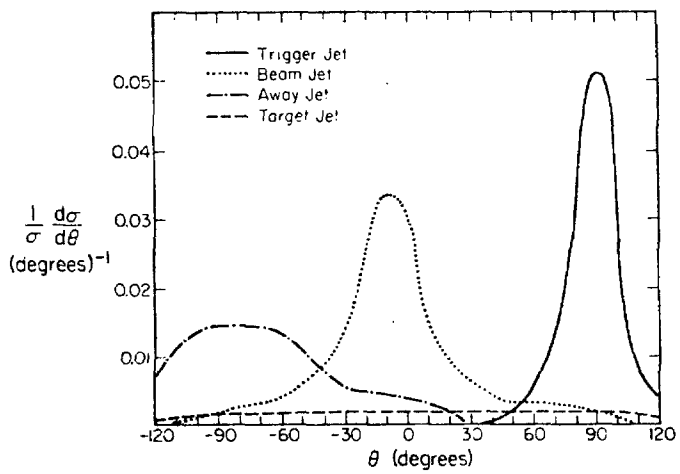

Figure I-4: Angular distribution of charged particles which are accepted by the E260 spectrometer and have energy greater than 0.5 GeV in the c.m. (From Reference 11).

etc.) or a quark-antiquark ($u\bar{d}$, $d\bar{s}$, etc.) system. Various theoretical models have predicted that the fragmentation of such systems should be independent of their color. We will be able to compare some of these systems.

Similar measurements for fragmenting gluons provide an important test of QCD. These measurements are difficult at PETRA as the gluon is produced by a hard bremsstrahlung and is therefore spatially accompanied by a quark. In hard hadron-hadron collisions, an incident gluon can be knocked out of a hadron without a quark accompanying it. Gluons produced in such a process may have reasonably high p_t at Tevatron energies, even though they are produced at relatively low x_t. Therefore, perturbative QCD will be applicable. Gluon jets will be tagged by using the technique of Reference 19.

Without going into details of specific theoretical models, there are a number of properties of quark and gluon fragmentation that should be measured.[20,21] For example, is the average multiplicity in a gluon jet larger than in a quark jet? Near $z = 1$,[22] does the gluon jet have a softer momentum spectrum than a quark jet? In the situation where $z_1 + z_2$[23] approaches 1, are the two fastest hadrons in a quark jet faster than the corresponding pair in a gluon jet? Is the opening angle of a gluon jet larger than that of a quark jet? Is ϕ production greater in a gluon jet? What is the height of the rapidity plateau for a gluon jet? What are the quantum numbers of gluon and quark jets?

The proposed experiment will use two Cerenkov counters (see Section II and Appendix B) to determine the identity of hadrons in the scattered jets. The range of z covered by these counters is discussed in Appendix B.

High-Mass Dimuon Events

The Dimuon Continuum: Drell-Yan Mechanism

Most of the experiments which have provided data on the Drell-Yan mechanism have triggered on high-mass dimuon pairs.[24] In order to obtain

sufficiently high detection rates these experiments have run in the so-called "closed geometry" wherein an iron absorber is placed close to the target and only the outgoing muons are detected.[25,26] An exception has been the open-geometry technique employed by Barate et al.[27] One of the results which has emerged is the discrepancy among experiments and between experiment and theory regarding the Drell-Yan cross section. References (25) and (27) report a cross-section which is twice as large as expected from the diagram of Figure I-1. Higher-order QCD diagrams for subprocesses such as those shown in Figure I-5 are thought to contribute.[28,29] Events described by subprocesses (a), (b) and (c) should give rise to a high-p_t dimuon pair and a parton (either quark or gluon) jet. Events described by subprocesses (e) and (f) will yield a high mass dimuon as well as two quark jets. Our excellent p_t acceptance for the dimuon (see Fig. IV-2) as well as our ability to identify particles in the high-p_t parton jets will allow us to make a systematic determination of the relative importance of the above subprocesses. The method proposed for triggering on events yielding high mass dimuons is described in Appendix E.

Production of the ψ

The dimuon mass spectrum shows not only the continuum, (which is the subject of above studies) but also significant resonance production (ψ and Υ). In the quark model the ψ and Υ are $c\bar{c}$ and $b\bar{b}$ states respectively. The mechanism of how such mesons are produced in collisions of hadrons which have very little c or b content is very interesting. The production of hadrons produced in association with the ψ will be studied in this experiment. For example we will study the difference (if any) in the character of jets accompanying dimuons in the continuum compared to the character of jets accompanying the ψ.

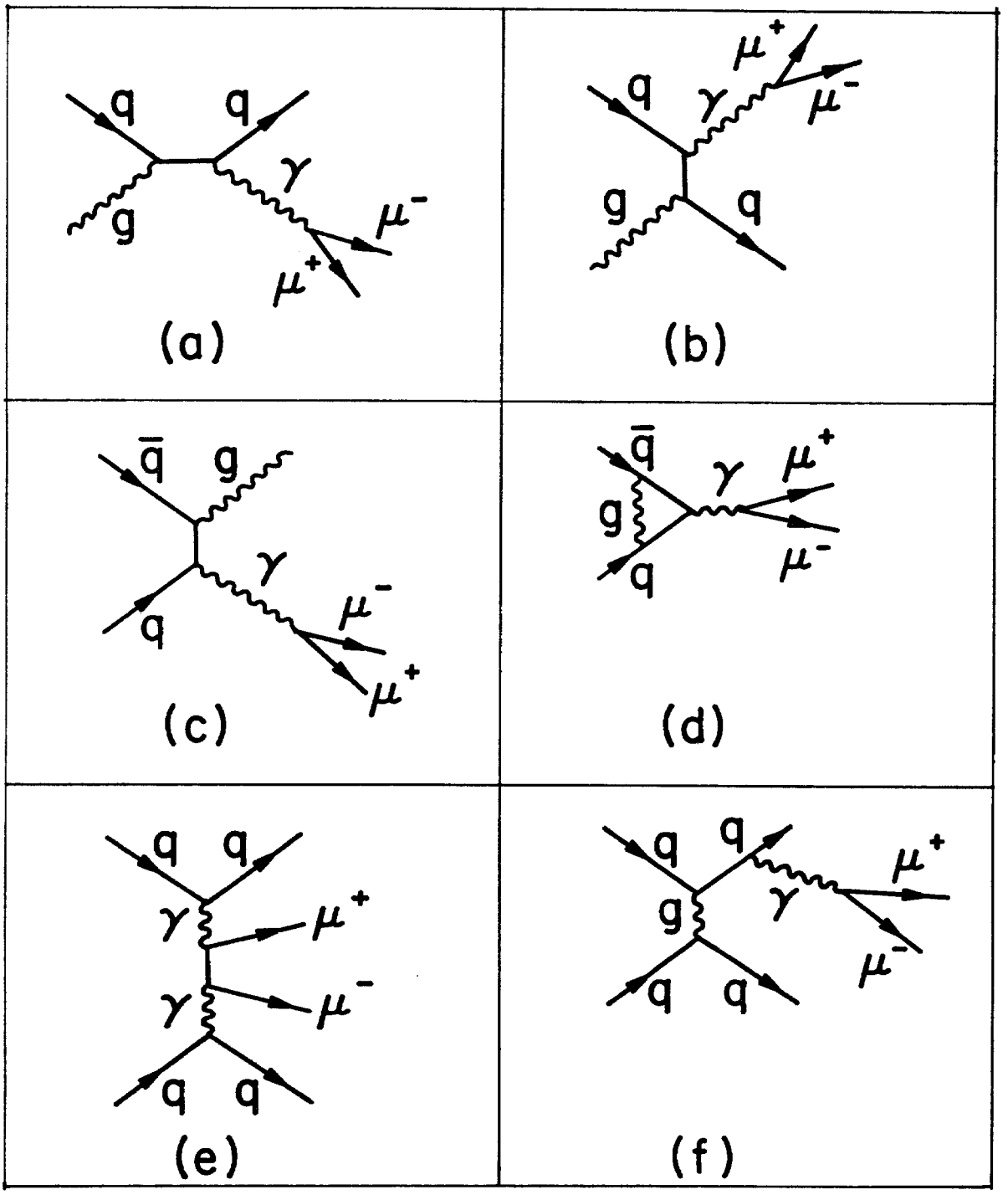

Figure I-5: (a) through (f) are second-order processes giving rise to high mass dimuons. (From Reference 29)

The production of ψ is observed to be about five times larger in $\bar{p}p$ collisions compared to pp collisions at 39.5 GeV/c incident momentum.[30] This suggests that $q\bar{q}$ fusion may be important in ψ production. However at higher incident momenta (150÷200 GeV/c) the ratio of ψ production in $\bar{p}p$ compared to pp is roughly 1.4.[29] This suggests that at higher energies the ψ might also be produced from an initial gg (gluon amalgamation) with the emission of a third gluon to conserve color. Thus the detection of a gluon jet in association with a ψ could provide a clue to the ψ production mechanism.

Forward Jets in High-p_t Jet and Dimuon Events

One of the unique aspects of the proposed experiment is the instrumentation to study, in detail, the parameters of the forward jet associated with the beam "spectator" partons. The details are presented in Section II and Appendices B and F. Particle type correlations between the forward jet and scattered jets and between forward jet and high-mass dimuons are especially interesting.[31-33] In order to make a thorough study of the forward jet correlations in these processes it is necessary to vary the incident beam type. In addition to proton beams we will also use $\pi^{\pm}$, $K^{\pm}$ and $\bar{p}$ beams.

To the extent that the diagram of Figure I-1 describes high-mass dimuon production, the existence of a high-mass dimuon tags the flavor of the forward-going jet. For example consider what happens if valence quarks are involved.[34] For the incident π^+, the $\bar{d}$ annihilates to produce the high-mass dilepton pair leaving the spectator u to fragment as a forward-going low-p_t jet. For an incident π^- the forward jet is initiated by a d quark while an incident K^- results in a forward s-quark jet. By studying the charge and other quantum numbers of the particles in the forward jet we will have a unique opportunity to test the various hypotheses for how low-p_t quarks fragment.

Tracking the characteristics of the beam jet as we move from sea-sea to sea-valence to valence-valence quark annihilation will be one of the major goals of this experiment. Appendix H lists the expected fraction of sea-sea, sea-valence and valence-valence quark annihilation for p_{inc} = 500 GeV/c and p_{inc} = 1 TeV/c.

Physics from Nuclear Targets.

The interest in using nuclear targets stems from the idea that nucleons within the nucleus will interfere with the evolution of partons into hadrons. Attempts have been made, both experimental[6,7,11,35] and theoretical[36-38], to study this phenomenon. At the moment there is no general consensus on the mechanism. More data is needed.

II. Description of Experiment

The proposed experimental layout is shown in Figure II-1. A large fraction of the apparatus already exists as the Multiparticle Spectrometer (MPS) facility currently being used for E557, E580 and E623.[39] Most of the additional items needed to carry out this experiment are associated with the dimuon trigger and a measurement of the characteristics of the forward jet.

Existing MPS and Minor Modifications

Much of the equipment shown in Figure II-1 already exists. An 18" long liquid hydrogen target is being used for E557 as well as a "nuclear" target consisting of 6 thin nuclear foils (different A) spread out over 18 inches (see Section III). PWC stations (see Appendix G), A, B, C, D and F already exist or are being built for presently approved experiments. The spectrometer magnet exists and will remain in place. Cerenkov counters $\check{C}_A$ and $\check{C}_B$ (see Appendix B) already exist. The box of $\check{C}_B$ will have to be lengthened. The calorimeter (CAL1 and CAL2 in Figure II-1) used to trigger on and measure high-p_t jets is being used in E557. This calorimeter will be moved downstream of the magnet by an additional 6 meters. The electronics associated with the calorimeter trigger, calibration system and monitoring system is being used for E557. Integral parts of this calorimeter system include a movable, computer-controlled table, a laser system and a dedicated LSI-11 for monitoring. More details on this system are given in Appendix D. A modification needed to carry out this experiment will be the addition of a top row and bottom row of modules necessitated by moving the calorimeter downstream. The additional modules are discussed in Appendix D. Measuring station E shown in Figure II-1 will be a drift chamber system, currently under construction for E623, which will

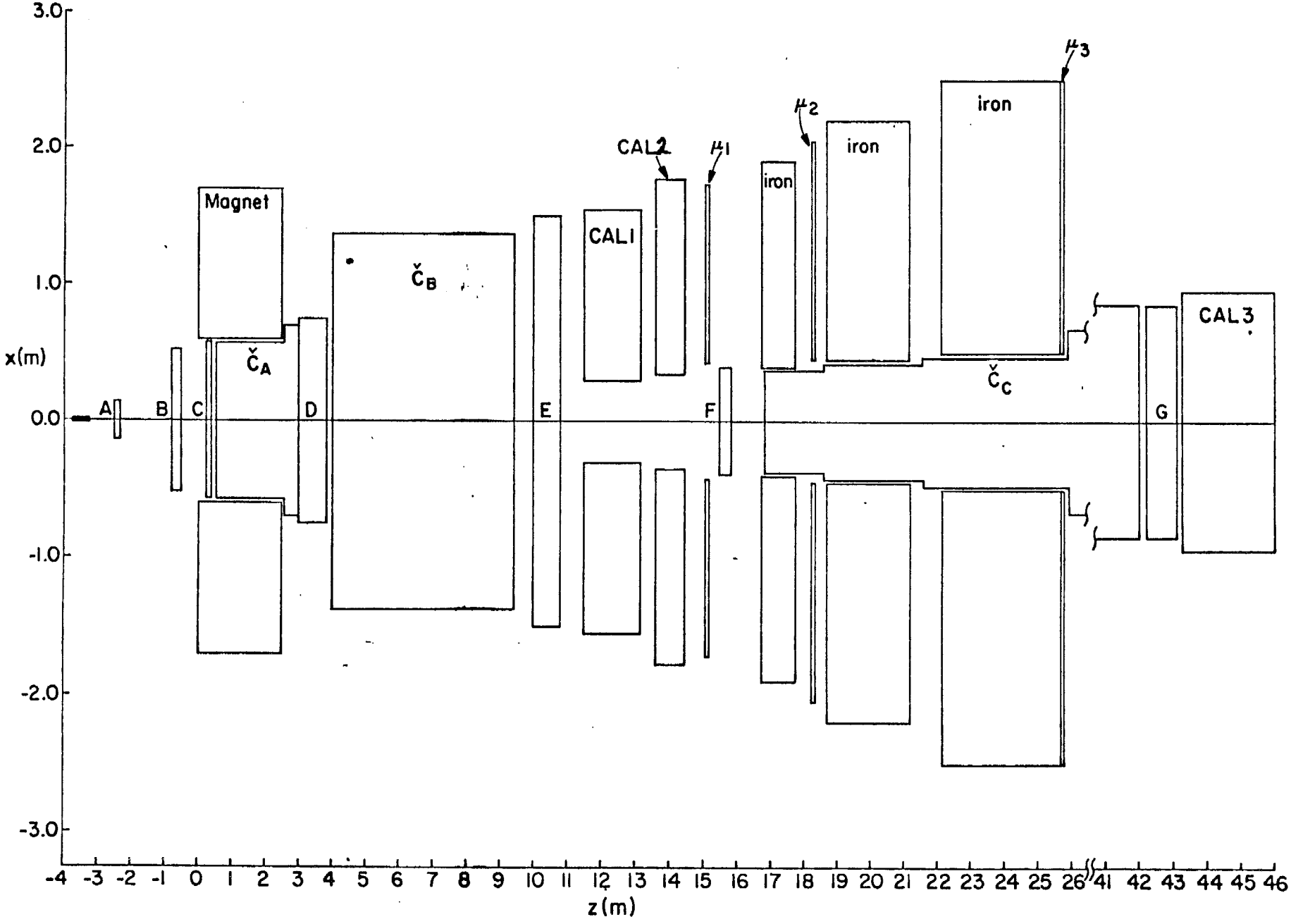

Figure II-1: Layout of the Multiparticle Spectrometer (MPS) as modified for the proposed experiment.

replace the spark chambers presently used in the MPS. Two stations, each with x, y and u planes are being built. In order to cover the necessary aperture for the proposed experiment the two stations will be staggered vertically. To regain the all important redundancy needed for pattern recognition we are requesting that Fermilab build two more stations identical to those currently being built.

Major Modifications to the MPS

In order to implement the dimuon trigger we will need to add 7 meters (~500 tons) of iron as an absorber. A scintillator hodoscope at μ_3 and PWC stations at μ_1 and μ_2 will also be added. The stations μ_1, μ_2, μ_3 along with a trigger processor which uses data from these stations to form the dimuon trigger are discussed in more detail in Appendix E.

In order to measure the characteristics of the forward jet a long Cerenkov counter, $\check{C}_c$ will be added. This counter is discussed in detail in Appendix B. Momentum measurement of charged and neutral particles in the forward jet will be carried out using a forward calorimeter (discussed in Appendix F). In order to track charged particles in the forward calorimeter and the $\check{C}_c$ mirror plane a PWC station G will be added. This station is also discussed in Appendix F.

The addition of $\check{C}_c$ and the forward calorimeter will require an extension to the existing MPS building. This extension consists of a 75 foot-long narrow building at ground level, wide enough to house the $\check{C}_c$ counter with a slightly wider downstream end to allow sufficient room to work on the forward calorimeter. A small excavation may be needed at the end of the present building.

We are studying several designs for an improved vertex detector. However, we have not yet decided whether it will be worthwhile to augment the current vertex detector, which consists only of a cylindrical PWC and cylindrical shower counter around the target.

Geometry for 500 GeV/c and 1000 GeV/c Running

This proposed experiment has been designed to run at two beam momenta: 500 GeV/c and 1000 GeV/c. The geometry is optimized for 1000 GeV/c running. For 500 GeV/c running the only part of the apparatus which moves is the target (which moves downstream by 2 m) with an associated accordion compression of the chambers in front of the analyzing magnet.

III. Triggers

We will have the following types of triggers:

A. Interacting Beam (1 trigger)

B. High-p_t Jet: (see Appendix D)

1. Single High-p_t Particle (2 triggers: LO and HI thresholds)
2. Di-jet (4 triggers: LO and HI for both TOP/BOTTOM, LEFT/RIGHT)
3. Global (2 triggers: LO and HI)

C. Dimuon (2 triggers: 2 values of θ_{min}) (see Appendix E)

In addition we may have 2 additional triggers in which the Global and Dimuon triggers also require a kaon requirement from the beam identification system (see Appendix A). Thus we will run with 13 triggers. Triggers with higher rates will be scaled down.

IV. Rate Calculations and Yields

In calculating estimated numbers of events the following assumptions are made:

1. Accelerator. E = 1000 GeV. A 20 sec long spill is delivered once per minute. Various inefficiencies reduce the 60 spills/hour to 50 spills/hour so a 1000 hour run has 50,000 spills.

2. Target. Calculations are made for two different targets, both 0.1 nuclear collision lengths in total thickness.

(a) An 18" long liquid H_2 target (.075 collisions lengths) plus entrance and exit windows plus one or two thin nuclear foils. (see Figure IV-1(a))

(b) Nuclear foil target: 6 foils spaced roughly 3.5" apart. (see Figure IV-1(b))

The foil thicknesses are chosen to give equal numbers of high p_t jet events. for each foil. For this calculation it is assumed that $\sigma \alpha A^{\alpha}$ where $\alpha = 1.5$. Recent experimental evidence indicated α may become larger than 1.5.[7] If α = 1.5 then the total number of high p_t events will be 7.5 times greater from target (b) than target (a) for the same integrated beam flux.

3. Beam momentum and intensity. Calculations are made for two different beam momenta: 500 and 1000 GeV/c. For 1000 GeV/c diffracted protons we propose to run at an intensity of 6.6×10^7 per spill or 3.3×10^6/sec. The incident beam from the energy doubler would be about 10^{10}/spill and the desired reduction obtained by adjusting the targetting angle on the MW target.

For 500 GeV/c π^- we would run at 1.0×10^8 or 5.0×10^6/sec. The reason the intensity is raised by $\frac{3}{2}$ is because the interaction probability is $\frac{2}{3}$ of that for protons. This keeps the interaction rate the same for positive beam and negative beam runs.

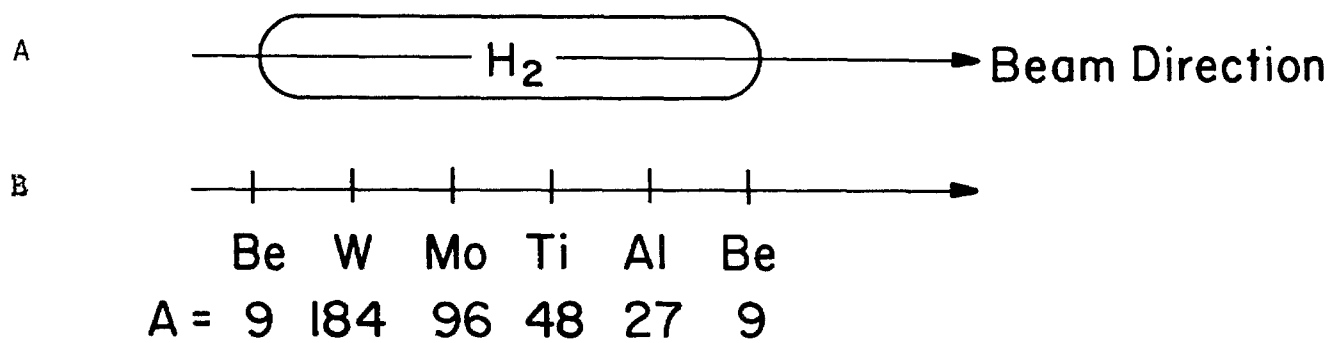

Figure IV-1 (a) Hydrogen Target (18 inches long)
(b) Corresponding Nuclear target showing foils of different A spaced out over 18 inches.

A 500 GeV/c positive run is of interest because it makes possible the comparison of π^- and π^+ induced jets as well as the determination of the s-dependence of proton induced jets.

For the 500 GeV/c negative runs we will require 3.3×10^{12} incident protons per spill. This will yield 1.0×10^8 π^- per spill. The K^- content of the negative beam is 1.1 percent while the $\bar{p}$ content is 0.13 percent. For the 500 GeV/c positive runs we will require 1.25×10^{11} incident protons per spill. The K^+ content is 1.7 percent. In calculating these numbers we assumed that the acceptance of the M6W beam is 2μsr and the primary target angle is 0 mrad.[40,41]

The choice of 500 GeV/c is a reasonable compromise between getting the highest possible energy on the one hand and proton economics on the other hand. The $K^\pm$ content of the beam is almost a factor of 2 higher at 500 GeV/c than 600 GeV/c so by tagging the incident K's (see Appendix A) reasonable statistics for studying s-quark jet production will be obtained. Finally at 500 GeV/c the π^+/p ratio is still high enough so the π^+-π^- comparison can be made.

4. Interaction rate and accidentals. With the above assumptions the interaction rate for all runs will be 3.3×10^5/sec. Multiple interactions can cause fake high p_t events.[42] The way this is dealt with was outlined in Section III.

The total integrated flux in a 1000 hour run will be:

$$F = \frac{3.3 \times 10^5 \text{ inter/sec} \times (50{,}000 \times 20) \text{ spill-sec}}{30 \text{ mb (inelastic)}} = 11000 \text{ ev/nb.} \quad \text{(IV-1)}$$

5. Jet cross sections. Using results from E260, E395, and NA5[43] for single jet production in pp collisions a formula for the invariant cross section is obtained that can be used for Tevatron rate estimates:

$$E \frac{d^3\sigma}{d\,p^3} = 7.1 \times 10^7 \; p_t^{\;-6.79} \; (1-x_t)^{9.52} \text{ nb/(GeV/c)}^2 \qquad \text{(IV-2)}$$

At high p_t incident $(q\bar{q})$ systems become considerably more effective at making jets than 3q systems. This effect has been measured in E260[11] and can be approximated as:

$$\frac{\sigma_{(\pi-K)p}}{\sigma_{(p+\bar{p})p}} = \frac{2}{3} \qquad \text{for } x_t < 0.3$$

?

$$= \frac{1}{(2.2 - 2.8\, x_t)} \qquad \text{for } 0.25 < x_t \leq 0.75 \qquad \text{(IV-3)}$$

$$= \text{large but unknown} \qquad \text{for } x_t > 0.75$$

6. Minimum p_t. To prepare tables of expected numbers of events in a 1000 hour run, one must also consider the magnitude of the off-line computing. For purposes of this proposal we have assumed that 3×10^6 events collected in a 1000 hour run is a reasonable amount. This translates to 60 events recorded in each 20 second spill. The other consequence of this total event limit is to impose a minimum threshold. Triggers may be used below this minimum but then prescaling will be used.

7. Acceptance and Resolution

$$\frac{dN}{dp_t^2} = E\,\frac{d^3\sigma}{d^3p}\,\frac{\Delta y \quad \Delta\phi}{2}\,F \qquad \text{(IV-4)}$$

We assume $\Delta y = 1.1\ \Delta\phi = 1.0 \times 2\pi$ and $\frac{dN}{dp_t} = ce^{-Kp_t^2}$ where K is approximately $3/(\text{GeV}/c)^2$.

Thus $N(p_t > p_{t\ min}) = 1.8 \times 10^{12}\ p_t^{-5.79}(1-x_t)^{9.52}\ f(x_t)$ events where $f(x_t)$ depends on particle type and ratio in beam. For protons $f(x_t) = 1$.

Finite resolution of the calorimeter will increase the number of triggers at $p_{t\ min}$ by a factor of 2 to 5. These additional triggers due to upward fluctuations will end up, after final analysis, in lower p_t bins.

8. Event Tables - High-p_t Jet Triggers

The expected yields for high-p_t jet triggers are given in Tables IV-1 and IV-2 (see next page). In these tables the column '$p_{t\ min}$' refers to the transverse momentum of a single jet. It, therefore, includes transverse momentum from soft gluon emission. In order to calculate the modulus of the transverse momentum of the di-jet system ('$p_{t\ di\text{-}jet}$') we have doubled $p_{t\ min}$ and subtracted 1 GeV/c (this assumes that gluon emission contributes .5 GeV/c to each parton).

Table IV-1

Yields for High-p_t Jets for p_{inc} = 1 TeV/c

p_t min (GeV/c)	P_t(di-jet) GeV/c	$N(p_t > p_{t\ min})$ 1000 hours p_{inc} = 1 TeV/c H_2 target	$N(p_t > p_{t\ min})$ 1000 hours p_{inc} = 1 TeV/c Multi-foil nuclear target
6	11	2.5×10^6	
7	13	5.6×10^5	4.2×10^6
8	15	1.3×10^5	9.8×10^5
9	17	3.2×10^4	2.4×10^5
10	19	8000	6.0×10^4
11	21	1900	1.4×10^4
12	23	470	3500
13	25	100	780
14	27	20	160

Table IV-2

Yields for High-p_t Jets for p_{inc} = 500 GeV/c

$p_{t\ min}$ (GeV/c)	P_t (dijet) (GeV/c)	proton events	π^+ events	K^+ events	π^- events	K^- events	$\bar{p}$ events
		$N(p_t > p_{t\ min})$ 1000 hrs p_{inc} = 500 GeV/c (positives) H_2 target			$N(p_t > p_{t\ min})$ 1000 hrs p_{inc} = 500 GeV/c (negatives) H_2 target		
5	9	3.1×10^5	4.7×10^5	4.9×10^4	4.3×10^6	4.8×10^4	7300
6	11	4.1×10^5	7.2×10^4	7600	6.7×10^5	7400	1000
7	13	5.8×10^4	1.2×10^4	1300	1.1×10^5	1200	130
8	15	7900	2000	220	1.9×10^4	200	20
9	17	1000	340	40	3100	40	
10	19	100	50		480		
11	21				70		

9. Dimuon Trigger. Running simultaneously with the various jet triggers will be the dimuon trigger discussed in Appendix E.

To determine the acceptance, the dimuon x and p_t were generated according to the 150 and 175 GeV/c results of Barate et al.[27]

$$\frac{d\sigma}{dx} \propto [1 - (x_F - .14)]^2 \qquad \text{for } -0.72 < x_F < 1. \qquad \text{(IV-7)}$$
$$= 0 \qquad \text{for } x_F < -0.72$$

and

$$\frac{d\sigma}{dp_t} \propto \left(1 + \left(\frac{p_t}{1.7}\right)^2\right)^{-3.2} \qquad \text{(IV-8)}$$

The dimuon decay was taken to be isotropic in the dimuon center of mass. The geometrical acceptance is shown in Figure E-3 (upper curves) as a function of dimuon mass. Figure IV-2 shows the x_F and p_t acceptances as a function of dimuon mass and beam momentum.

To calculate the 500 GeV/c π^- yield we used the Drell-Yan cross section, which is given explicitly in the above reference; no sea quarks were used. For π^+p, the cross section (without sea quarks) is down by a factor of two (neutron target) or eight (proton target). However, since $\frac{M_{\mu\mu}}{\sqrt{s}} \approx .1$ even for $\mu\mu$ masses of 10 GeV, clearly we will be probing the pion and nucleon seas. Thus for both π^+N and pN interactions we expect a cross section at 500 GeV/c only a little smaller than for π^-p. The 1000 GeV/c yield estimates are also based on the initial state being π^-p but we feel they are reasonable considering sea-sea interactions become even more important as s increases. The table of yields is given below. Note that none of the yields contains the factor of 2 by which the Drell-Yan cross section is too low; this effect, due to higher order processes, was first pointed out by a subgroup of this collaboration.[27] For the ψ and Υ a cross section times $\mu\mu$ branching ratio of 7nb and 7pb respectively were assumed. For the nuclear target $\sigma \propto A^{1.0}$ was assumed.

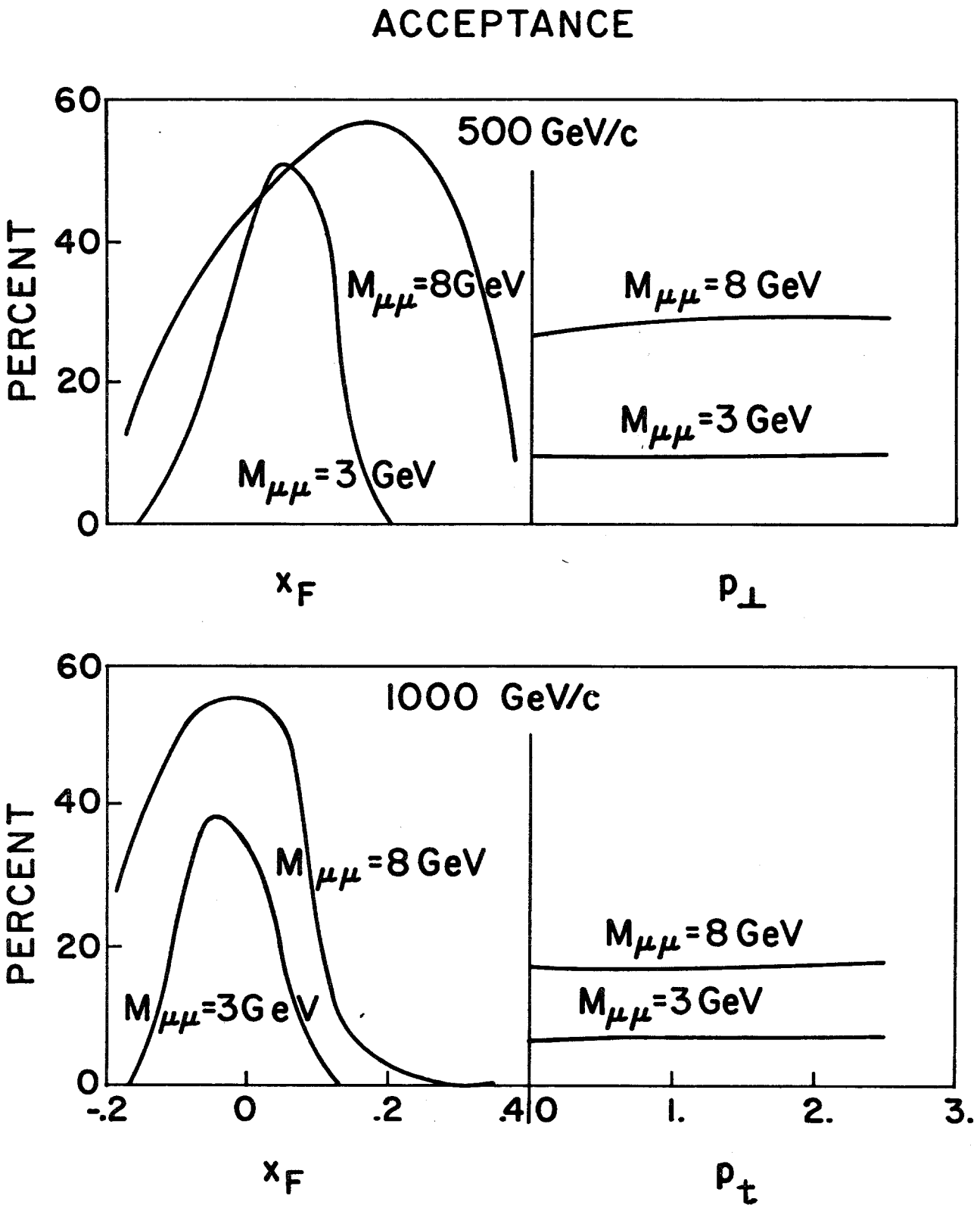

Figure IV-2: x_F and p_t acceptance for $M_{\mu\mu}$ = 3 GeV and $M_{\mu\mu}$ = 8 GeV shown for p_{inc} = 500 GeV/c and p_{inc} = 1000 GeV/c

Table IV-3

Dimuon Yield

	p_{inc} = 500 GeV/c (π) Yield/1000 hours		p_{inc} = 1 TeV/c (p) Yield/1000 hours	
	Target		Target	
Mass	H_2	Nuclear	H_2	Nuclear
ψ	5500	8200	3500	5000
3-5 GeV	1000	1500	700	1000
5-7 GeV	400	600	300	400
7-9 GeV	130	200	120	180
Υ	20	30	10	15

10. Run Plan. The above tables show the numbers of jets events and dimuon events for 1000 hour data runs under 6 possible running conditions: 3 beam energies/polarities and two different target arrangements.

We request initial approval at 2000 hours plus 500 hours of tuneup. The 2000 hours would be apportioned by us among the various possibilities mentioned.

V. Analysis

We are requesting 2000 hours of beam time. We expect to collect about 5.5×10^6 jet triggers and 4.0×10^6 dimuon triggers for a total of 10^7 triggers.

A software package already exists for reducing raw data from the MPS including track finding. This software package (TEARS) has evolved since its initial use in E260 and E110. TEARS has been updated for use in E557 and in E580 and it now contains routines to analyze data from the E557 calorimeter. We expect the modifications necessary to analyze data from the proposed experiment to be straightforward. Based on our experience we would expect that each trigger will require about 4 sec of analysis time using a VAX-11 computer. Various groups in the collaboration already have or will soon have a VAX-11 dedicated for analysis about half-time. Thus we expect to be able to reduce the data using the collaboration's computer resources in about 1-2 years. Since the data are likely to be collected in at least 2 data runs separated by several months to a year the analysis of 10^7 triggers is certainly manageable.

VI. Comparison with other Experiments

Other experiments measuring high-p_t jets and high-mass dimuon production are currently in progress or being planned at Fermilab, PETRA, PEP and CERN. We discuss several of these briefly and point out how this proposed experiment compares to these experiments.

1. E557 (FNAL), E609 (FNAL), NA5 (CERN)

These experiments measure high-p_t jet production in reactions initiated by 300 GeV/c mesons and 400 GeV/c protons. Jets with $p_t < 8$ GeV/c are measured.

Proposed Experiment: We will study jets in reactions initiated by 500 GeV/c mesons and 1000 GeV/c protons. In the latter jets with $p_t < 14$ GeV/c will be measured. A much more detailed measurement of the forward jet will be made. The dimuon trigger allows one to tag the flavor of the quark initiating the beam jet.

2. PETRA, PEP

Experiments at PETRA and PEP will study jets in the momentum range $\approx$15 GeV/c.

Proposed Experiment: We will study jets with comparable p_t. However this experiment allows one to look at jets initiated by hadrons with different species. Also the jets produced in hadron-hadron collisions are due to a very different class of subprocesses which can only be studied in hadron-hadron collisions. Comparison of e^+e^- produced jets and hadron-hadron produced jets is important.

3. E605 (FNAL), NA-10 (CERN)

These experiments measure dimuon production in a closed (NA-10) or semi-closed geometry using very intense beams.

Proposed experiment: We cannot compete with these experiments in terms of rate. However since we detect the hadrons associated with dimuons we can study the details of dimuon production (see Section I).

4. NA-14 (CERN)

This is an open geometry dimuon experiment using a 150-200 GeV/c photon beam.

Proposed experiment: We will complement this experiment by using incident π, K and p beams. Also the proposed experiment will run with higher incident momenta.

Summary

In summary the proposed experiment has the unique feature of doing a detailed study of the beam jet produced in association with dimuons or high-p_t jets. For this reason an open geometry experiment is necessary. Since the correlations between incident beam hadron and the forward going jet are important we need to do a fixed-target experiment in a beam with sufficient $\pi^{\pm}$, $K^{\pm}$ and $\bar{p}$ flux in addition to protons. Finally the nature of the hard scattering processes we wish to study dictates that we use the highest energy meson beams and proton beams available. For all these reasons the proposed experiment complements and extends the range of parton-parton physics being studied by current experiments or experiments soon to run at FNAL, CERN, the ISR, PETRA or PEP.

VII. Requests for Resources from Fermilab

A. The major requests from Fermilab include:

1. 500 GeV/c positive and negative beams and a 1 TeV/c diffracted proton beam, all of sufficient intensity (see Section IV);
2. Two sets of drift chambers in addition to those being constructed for E623 (see Section II and Appendix G);
3. Aid in locating, moving and rigging of the iron absorber (~500 tons, see Section II and Appendix E);
4. Extension to the MPS building wide enough to house $\check{C}_c$ and the forward calorimeter (see Section II). This extension will be above ground. Some excavation at the rear of the present building might be necessary;
5. Sufficient computer time on the Fermilab computer system to completely analyze ~10% of the triggers. We estimate that this will require between 1.0 and 1.5 seconds of Cyber time per trigger. We hope to analyze about 10^6 triggers at Fermilab.
6. Electronics from PREP in addition to the current E557 and E623 allocation from PREP. This includes readout system for the drift chambers, and 200 additional ADC channels to instrument $\check{C}_c$, the forward calorimeter and the expanded trigger calorimeter;
7. Delay cables and shift register electronics associated with instrumenting ~4500 additional PWC wires (see Appendix G).

B. Minor requests from Fermilab include:

1. Liquid H_2 target;
2. Superconducting spectrometer magnet cooldown;
3. Extension to the $\check{C}_B$ box (see Appendix B);
4. Box for $\check{C}_c$.

C. Experimenters will provide:

1. Additional PWC's (see Appendix G);
2. Vertex detector (as yet unspecified);
3. $\check{C}_c$ (threshold or ring-imaging counter; see Appendix B);
4. PWC stations (μ_1 and μ_2), scintillator hodoscope (μ_3) and electronics associated with the dimuon trigger processor (see Appendix E).
5. Forward calorimeter (see Appendix F).

Appendix A

Beam Identification at 500 GeV

We discuss here the beam type identification at 500 GeV/c. The existing transition radiation detector (TRD)[44] and Cerenkov counters used in E557 will be used without any major changes. The parameters of the TRD are given in Table A-1 while the parameters of the Cerenkov counters (all helium-filled) are given in Table A-2.

Table A-1

Transition Radiation Detector Parameters		
1600 Li foils -- 1.5 mil. in each of 2 radiators		
Pilot B Scintillator -- all in vacuum		
threshold for π^+ signal	20 Ke	in either radiator
threshold for π^- signal	15 Ke	in either radiator
threshold for $K^+ + \pi^+$	5 Ke	require both radiators
threshold for $K^- + \pi^-$	7 Ke	in either radiator

Table A-2

Beam Cerenkov Counters				
Counter	Length (m)	Refractive Index (He)	$N_{pe}(K)$	Efficiency
$\check{C}_o$	18.		1.05	.65
$\check{C}_1$	31.5	$1 + 1.76 \times 10^{-6}$	1.84	.84
Pruss	30.0		1.75	.83
Total	79.5			.99

The task of particle identification is different for positive and negative beams because the particle ratios are different for the two cases. Hence we discuss them separately.

The negative beam composition is ~99% π^-, ~1% K^- and ~0.1% $\bar{p}$. The TRD will be used to distinguish π^- from K^- and $\bar{p}$ since π's will usually produce a signal above a relatively high threshold (see Figure A-1). Information from the TRD will be used in conjunction with information from the Cerenkov counters to distinguish K^- from $\bar{p}$. The expected results are shown in Table A-3.

The positive beam composition is ~79. % p, 19% π^+ and 1.7% K^+. A different set of thresholds is chosen and the results given in Table A-3 and Figure A-2.

Table A-3

Purity of tagged beam						
	π^+	K^+	p	π^-	K^-	$\bar{p}$
all	19%	1.7%	80%	99%	1.1%	0.13%
labeled π	100%	---	---	100%	---	---
labeled K	<.01%	62%	38%	0.3%	99%	0.5%
labeled p	---	2%	98%	---	0.3%	99.7%

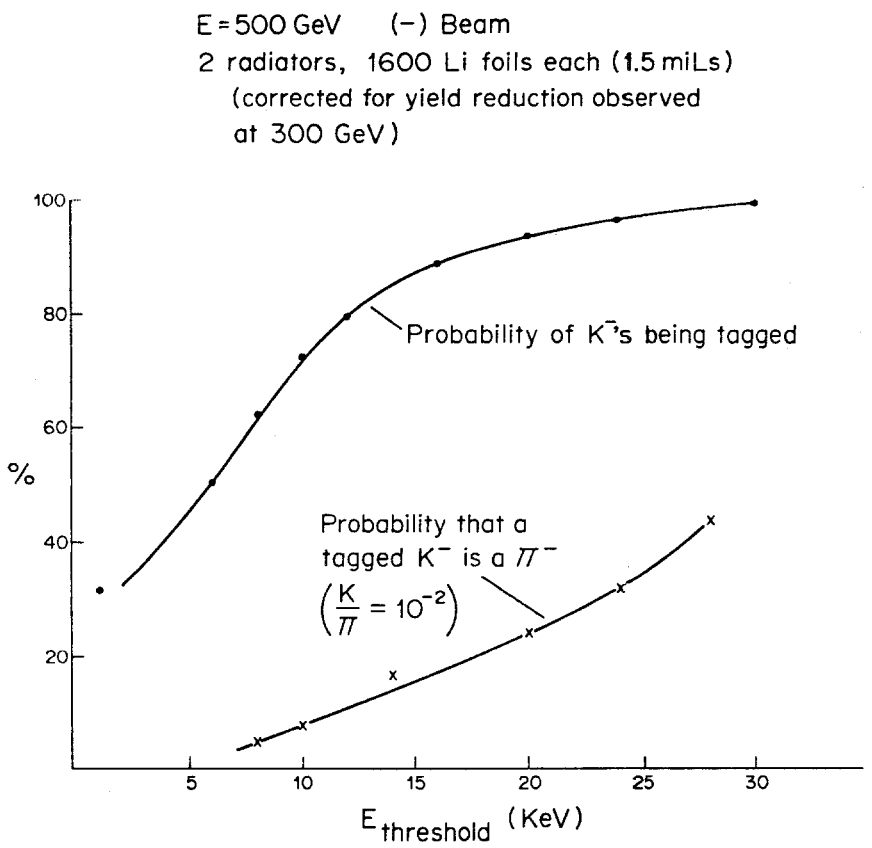

Figure A-1: Performance of the TRD for particle identification for a negative beam.

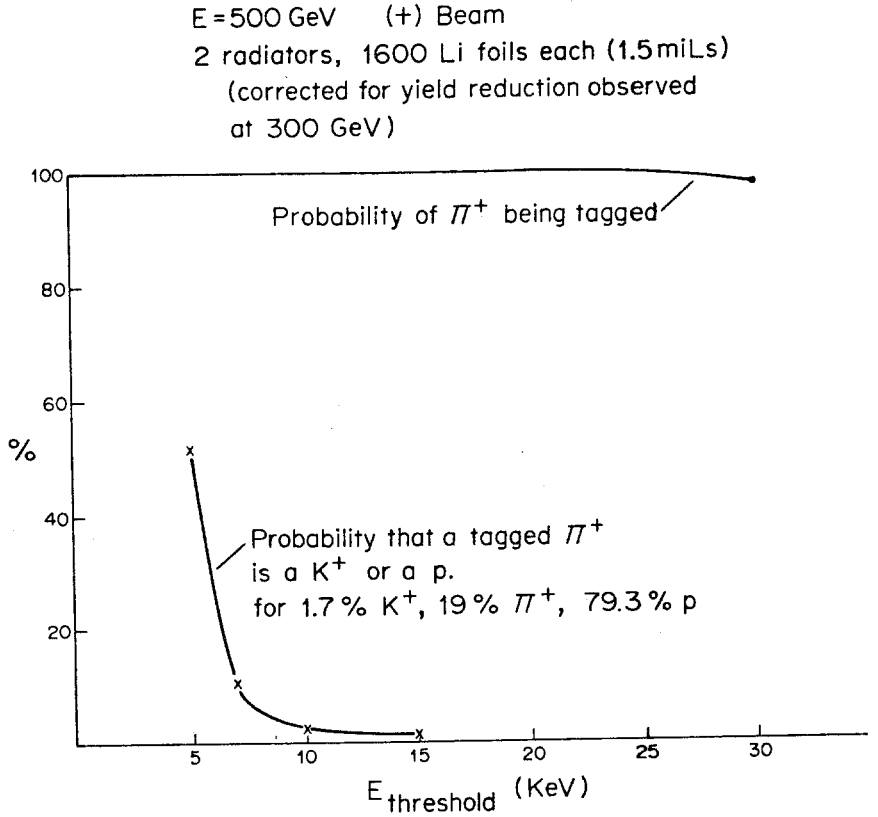

Figure A-2: Performance of the TRD for particle identification for a positive beam.

Appendix B

Secondary Charged Particle Identification

Identification of secondary charged particles produced in high-p_t jet and dimuon events will be accomplished using three segmented threshold Cerenkov counters: $\check{C}_A$, $\check{C}_B$ and $\check{C}_c$ (see Figure II-1). Each of these counters will operate at atmospheric pressure. $\check{C}_A$ and $\check{C}_B$ will be used in conjunction to identify particles associated with jets emitted at large angles in thec.m. while $\check{C}_c$ will be used to identify particles in the beam jet.

$\check{C}_c$

We are considering the possibility of using a ring imaging Cerenkov counter for $\check{C}_c$. Whether we do or not will depend on developments in this area. We currently plan to use a conventional segmented Cerenkov counter, C_c.

The purpose of $\check{C}_c$ will be to identify charged particles in the beam jet. The latter is characterized by high momentum hadrons in the laboratory contained in a forward cone of half-angle ~20 mrad. $\check{C}_c$ will be 26 meters long and filled with helium at atmospheric pressure. The relevant parameters for He as a radiator are given in Table B-1.

Table B-1

Parameters for He, Ne and N_2			
Parameter	He	Ne	N_2
n	1.000035	1.000067	1.000300
$P_{thres}(\pi)$ (GeV/c)	16.7	12.0	5.7
$P_{thres}(K)$ (GeV/c)	59.4	42.8	20.2
$P_{thres}(p)$ (GeV/c)	112.6	81.0	38.3
$\theta_{\beta=1}$ (mr)	8.4	11.6	24.5

The mirror plane for $\check{C}_c$ will be located 42 meters from the target and will be divided into 32 cells as shown in Figure B-1. The numbers given in the cells of Figure B-1 are the mean momenta of charged particles entering the cell and the fraction of times a charged particle is unaccompanied by another charged particle in the same cell ("singe occupancy fraction") regardless of momentum. The radius of the circle of the Cerenkov light cone intercepted at the mirror plane for a $\beta = 1$ particle is 22 cm. Thus finer segmentation of the mirror plane would be inappropriate. Pulse height analysis will be used to separate π's, K's and protons. For a $\beta = 1$ particle we expect 20 photoelectrons (n_{pe}) if we assume:

$$n_{pe} = 115\ L\ \theta^2 \qquad \text{(B-1)}$$

where L is the radiator length in cm and θ is the half-angle of the Cerenkov light cone. The expected laboratory momentum range for performing π, K, p separation using only $\check{C}_c$ is given in Table B-2.

Table B-2

Momentum and z-Range Over Which Particles are Identified Using $\check{C}_c$			
QUANTITY	π	K	p
$P_{laboratory}$ (GeV/c)	20-120	60-120	60-240
$P_{c.m.}$ (GeV/c)	0.5-3	1.5-3	1.5-6
$z(\equiv p/p_{JET},\ p_{JET} = 10$ GeV/c)	0.05-0.3	0.15-0.3	0.15-0.6

In Table B-2 we also show the corresponding c.m. momentum range as well as the $z(z \equiv p/p_{JET})$ range for a 10 GeV c.m. jet. The c.m. ranges are calculated assuming an incident momentum of 800 GeV/c, which is approximately half-way between the two proposed operating momenta of 500 GeV/c and 1000 GeV/c.

ONE QUADRANT OF $\check{C}_C$ MIRROR PLANE

CELL SIZE: 20CM X 40CM

AVERAGE MOMENTUM (GEV/C) →	24	23	23	23
SINGLE OCCUPANCY FRACTION →	0.98	0.97	0.95	0.94
AVERAGE MOMENTUM (GEV/C) →	23	24	46	80
SINGLE OCCUPANCY FRACTION →	0.96	0.93	0.88	0.82

BEAM LINE

Figure B-1: Segmentation of one quandrant of the $\check{C}_c$ mirror plane.

In the four-jet picture a typical jet has energy $\frac{1}{4}\sqrt{s}$ = 10 GeV in this case. As was pointed out in Section I the primary interest is in the higher-z particles of the jet.

We now discuss the π/K separation using $\check{C}_c$. The K threshold momentum is 60 GeV/c. However the range of momenta over which π/K separation can be accomplished will be extended to 120 GeV/c using pulse height analysis. The actual fraction of K's in the final sample of data identified as K's will depend on where one chooses to make the photoelectron cut (on the K requirement) and on the actual ratio of π to K. To illustrate the problem, in Figure B-2 we plot the distribution of number of photoelectrons, n_{pe}, for $\langle n_{pe}\rangle = 20$ and for $\langle n_{pe}\rangle = 10$. For a momentum of 80 GeV/c a π would yield $\langle n_{pe}\rangle = 20$ and a K would yield $\langle n_{pe}\rangle = 10$. We assume, in our example, that the actual π/K ratio is 5/1. We consider as a possible criterion for making a cut on the number of photoelectrons the value of n_{pe} where the Poisson curves intersect (see Figure B-2). The results are shown in Figure B-3 where we assume three different ratios of π/K (independent of momentum). What is plotted is the fraction of K's correctly identified in the final data sample.

Since the proton threshold is twice the kaon threshold, we can extend the range of momenta of identified protons out to 240 GeV, assuming a favorable $\pi K/p$ ratio. This is especially important since the distribution of leading protons in jets is not well understood.

The mirrors in the mirror plane of $\check{C}_c$ will have a focal length of 2 meters, which will give us an image size of 5 cm diameter. Thus 2 inch phototubes with Winston cones will be adequate for light collection.

$\check{C}_B$

The $\check{C}_B$ counter will be used to identify the higher momentum secondaries in the high-p_t jets, in the angular range 20 to 110 mrad (35° to 122° in the hadron-hadron c.m. for p_{inc} = 500 GeV/c, 50° to 138° for 1000 GeV/c).

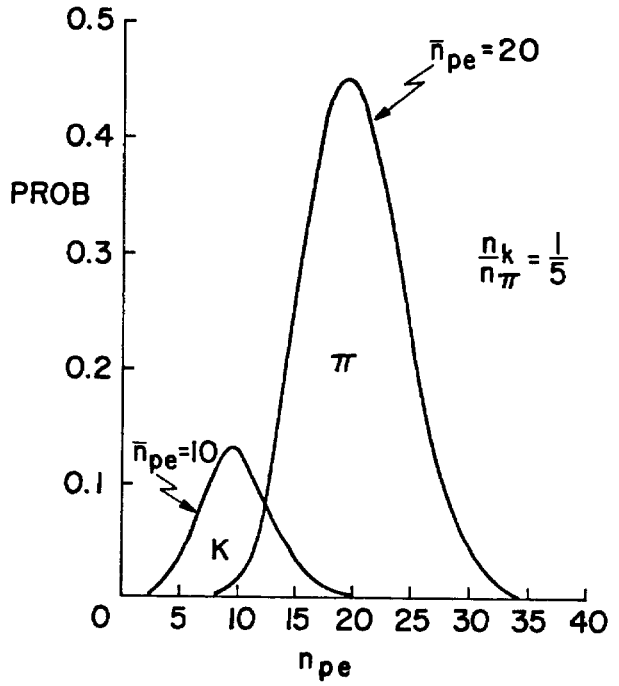

Figure B-2: Photoelectron yield for counter $\check{C}_c$ for π and K assuming p = 80 GeV/c and a ratio of $K/\pi = 1/5$.

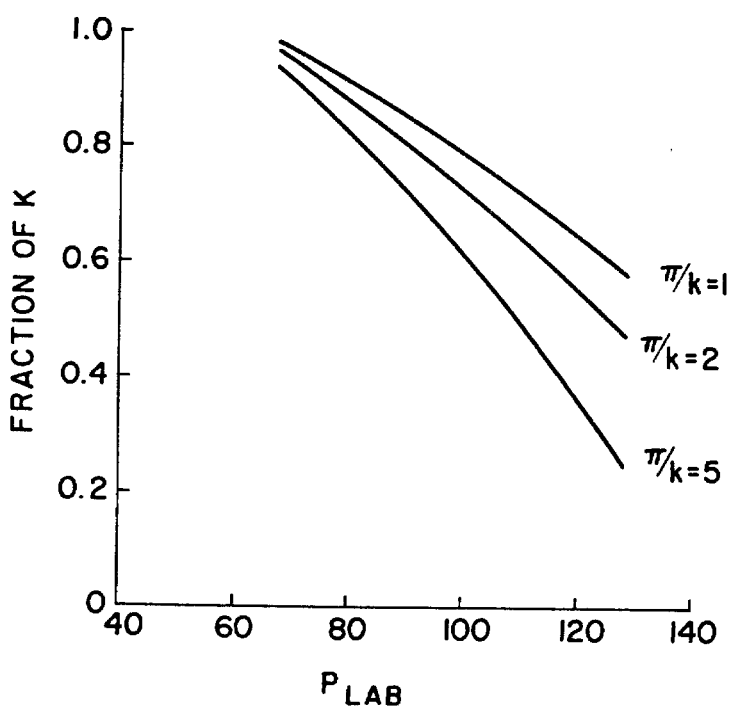

Figure B-3: Fraction of correctly identified K for different initial π/K ratios using as a photoelectron cut the value of the n_{pe} where the Poisson curves intersect.

Because the counter is limited to a length of 5.6 meters, $\check{C}_B$ will require a Ne fill in order to obtain a π/K separation that is comparable to the one obtained in $\check{C}_c$. Using Ne (see Table B-1) a $\beta = 1$ hadron traversing the full 5.5 meters of the counter will produce on the average 7.7 photoelectrons. Using the pulse height technique described previously we will (see Figure B-4) be able to separate K's from π's up to 60 GeV/c in the laboratory (p_t = 3 GeV/c, z = 0.3 for a 10 GeV jet at 90° (c.m.) at Tevatron energies.) Similarly, protons will be identified up to 120 GeV (p_t = 6 GeV/c, z = 0.6).

The granularity of the present MPS $\check{C}_B$ counter will be adequate for particles in the range 40 to 110 mrad. The Cerenkov light cone will be 8 cm in diameter on the mirror plane. In Fig. B-5 we show the probability of single occupancy for each mirror, that is that a charged particle crossing a mirror is unaccompanied by another charged particle in the same mirror. The probability rises from 80% at 40 mrad to 100% at 110 mrad. The average momentum for each cell is also given.

$\check{C}_A$

The purpose of $\check{C}_A$ is to complement $\check{C}_B$ and to identify the low z end of the hadron spectrum fragmenting from the scattered partons. $\check{C}_A$ and $\check{C}_B$ are matched, so that we can cover the momentum range shown in Table B-3. The equivalent p_t's are for Tevatron energies.

Table B-3

Momentum range covered by $\check{C}_A$ & $\check{C}_B$			
	π	K	p
P(GeV/c)	6 - 60	20 - 60	20 - 80
p_t (GeV/c)	0.3 - 3	1 - 3	1 - 4
z (p/p_{jet}, P_{jet} = 10 GeV/c)	0.03 - 0.3	.1 - .3	.1 - .4

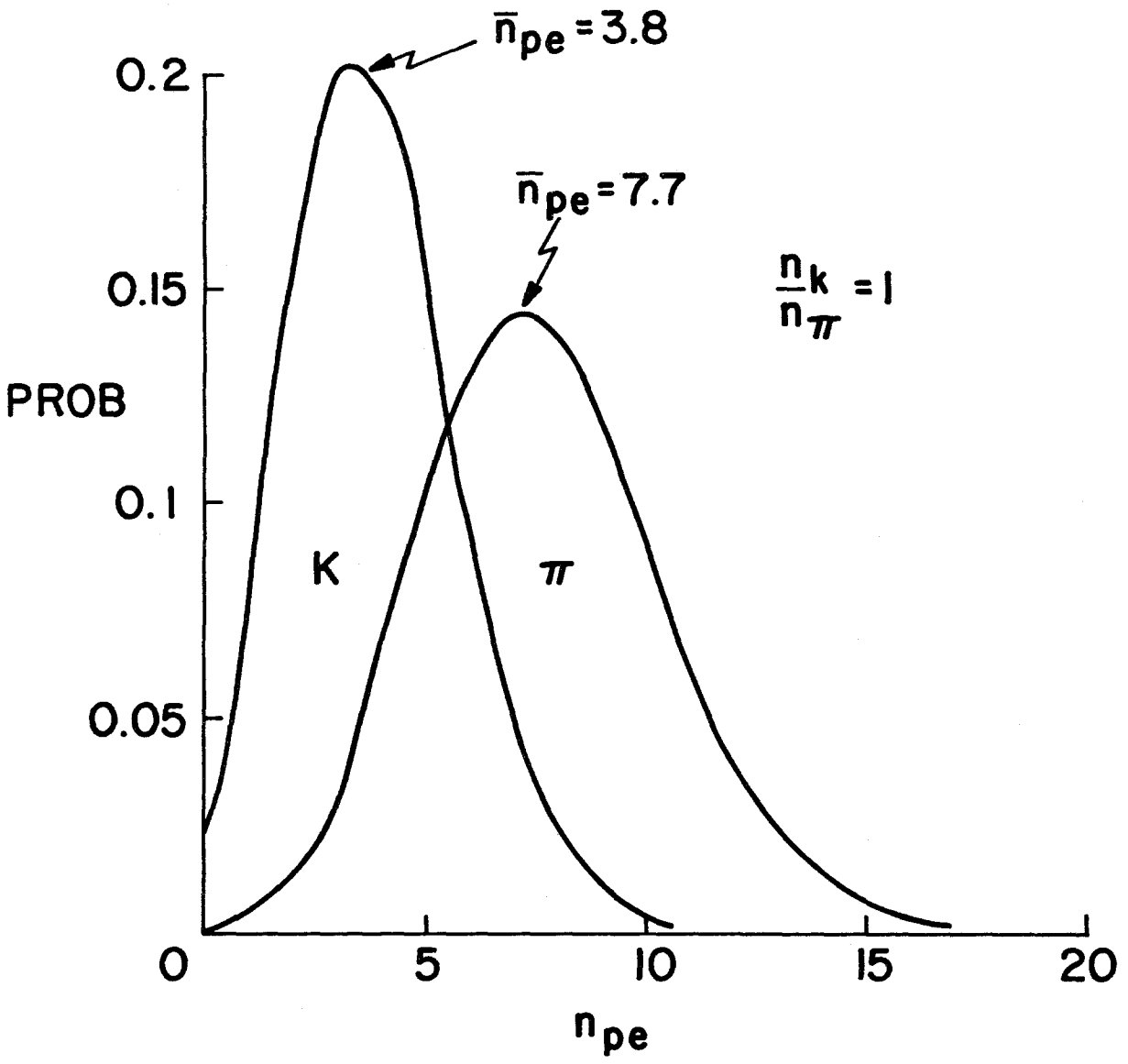

Figure B-4: Photoelectron yield for counter $\check{C}_B$ for π and K assuming $\beta = 1$ and a ratio of $K/\pi = 1$.

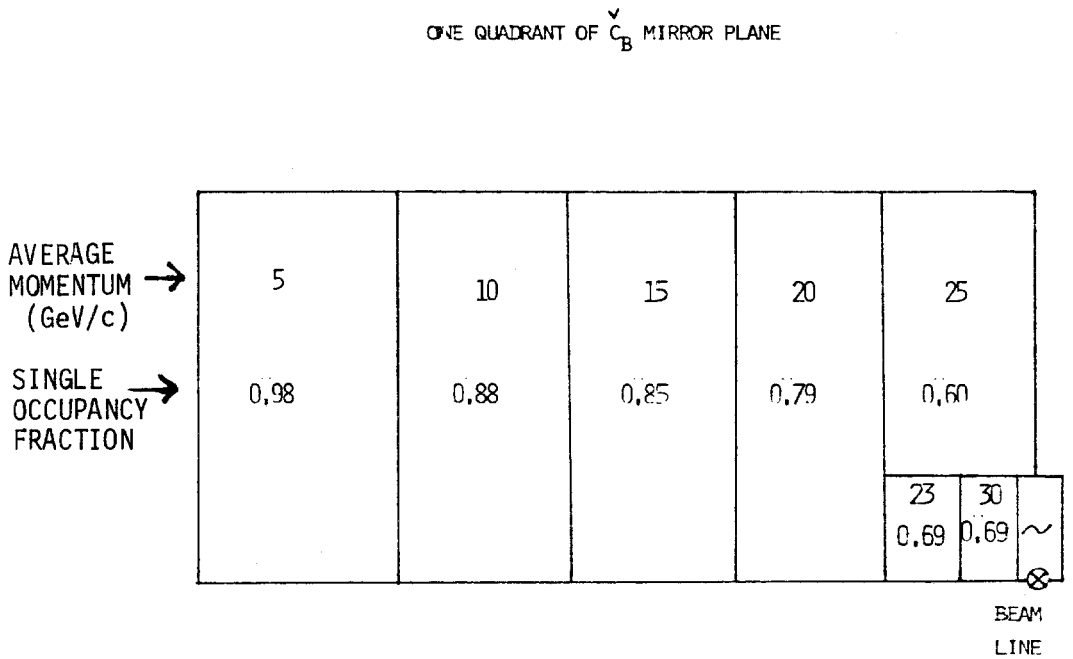

Figure B-5: Segmentation of one quadrant of the $\check{C}_B$ mirror plane.

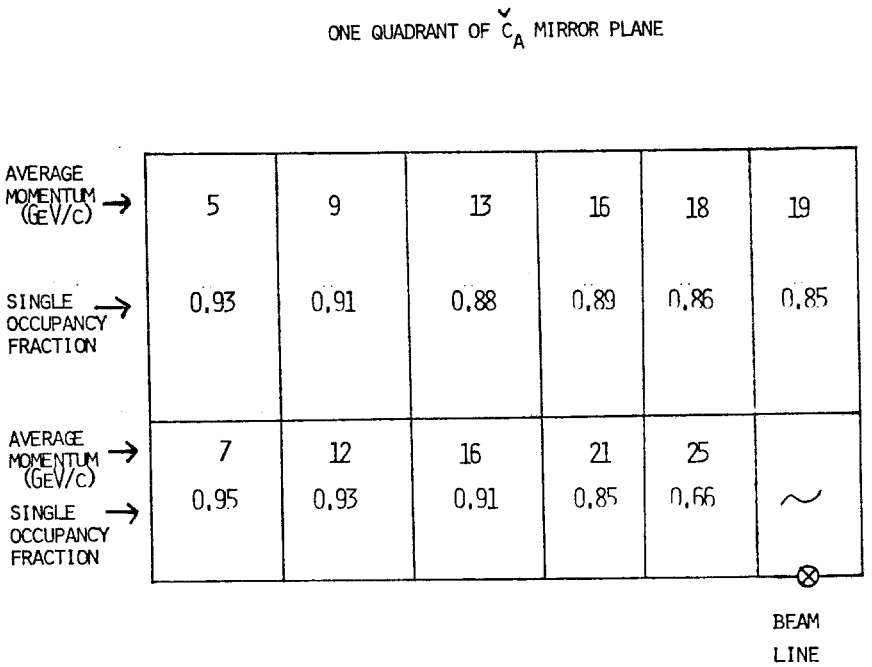

Figure B-6: Segmentation of one quadrant of the $\check{C}_A$ mirror plane.

The extension to lower z is achieved by a N_2 fill (see Table B-1) in the existing MPS 1.8 meter counter that is presently in place in the spectrometer magnet. For $n_{pe} = 110\ L\theta^2$ we will obtain an average of 12 photoelectrons for a $\beta = 1$ particle. The Cerenkov light cone will be 5.5 cm in diameter on the mirror plane.

The percentage of single occupancy using the current mirrors but evaluated at Tevatron energies is shown in Fig. B-6. Other than for the mirrors on the beam line, the resolution is quite good. The average momentum for each cell is also given.

Appendix C

Spectrometer Resolution

The resolution of the spectrometer with respect to magnetic momentum analysis of charged particles is discussed in this appendix. The resolution is discussed separately for the 500 GeV/c and 1000 GeV/c running conditions and for both narrow angle and wide angle tracks. Most of the particles in the beam jet will be emitted within a small cone (half-angle $\approx$ 20 mr) and with large momenta. For momenta greater than some critical momentum p_c ($\approx$ 130 GeV/c) the momentum measurement obtained using the forward calorimeter will be more accurate than that obtained using magnetic momentum analysis. This assumes $\Delta E/E = 0.7/\sqrt{E(\mathrm{GeV})}$ for the forward calorimeter. Above p_c we will determine the sign of the charge of the particles in the beam jet from their magnetic deflection.

Downstream Spectrometer

The geometry of the portion of the spectrometer downstream of the spectrometer magnet will remain fixed for 500 GeV/c and 1000 GeV/c running (refer to Figure II-1). Several PWC's will be added to the MPS as currently configured for E557. See Appendix G for the full list of existing and proposed measuring stations, including those which already exist, are being built or are being proposed. A PWC with 1 mm wire-spacing (part of the D-station) will be placed 1.4 m downstream of the magnet midplane. This chamber will have 320 vertical wires supported on a frame which is larger than the magnet aperture. A set (x, y, u planes) of PWC's (F-station) with 2 mm wire-spacing will be located 15.5 m downstream of the magnet midplane. These chambers will be used to locate the very forward tracks in the beam jet, as the drift chambers will not be able to resolve multiple hits in a cell. The angular resolution of this system of PWC's will be 0.11 mr and the spatial resolution of trajectories

projected to the magnet midplane will be $\approx$0.8mm. This latter number is pertinent because matching to points in the magnet midplane is the tightest constraint on the upstream trajectory.

The wide-angle tracks in the downstream spectrometer will be defined by the drift chambers and the D station (see Figure II-1) which is a set of 2mm wire-spacing PWC's located 1.5m downstream of the magnet midplane. If we assume a spatial resolution of 200μ for the drift chambers, the angular resolution of these wide angle tracks will be determined by the distance from the D station to the drift chambers (about 7.0 m) and spatial resolution of the D station PWC's. Thus the angular resolution for wide angle tracks in the downstream section of the spectrometer is expected to be 0.2mr.

The angular resolution, σ, for downstream trajectories for narrow-angle and wide angle tracks are summarized in Table C-1.

The angular resolution of the upstream portion of the spectrometer is defined by the fit to the vertex and the match at the magnet center and, of course the lever arm. Results from E557 indicate that the vertex can be fit, in the transverse directions, to about 0.2mm. The precision in the beam direction is not as good (about 3mm) but enters the angular precision in proportion to the sine of the production angle of secondary particles. This varies from negligible for the forward jet to about .3mr for the widest angles. The planned lever arms are 2.75m at 500 GeV/c and 4.75 at 1000 GeV/c. All these combine to yield the upstream angular resolutions given in Table C-1.

Table C-1

Angular Resolution, σ, of Charged Particle Trajectories		
	σ(500 GeV/c)(mr)	σ(1000 GeV/c)(mr)
Narrow-Angle, Downstream	0.11	0.11
Wide-Angle, Downstream	0.20	0.20
Narrow-Angle, Upstream	0.26	0.15
Wide-Angle, Upstream	0.52	0.30

The spectrometer magnet current will be set to impart a p_t kick of 0.2 GeV/c and 0.4 GeV/c for the 500 GeV/c and 1000 GeV/c runs respectively. Thus we expect to obtain the following resolution in momentum measurement:

	500 GeV/c	1000 GeV/c
$\Delta p/p$ (narrow angle tracks)	1.4×10^{-3} p	$.46 \times 10^{-3}$ p
$\Delta p/p$ (wide angle tracks)	2.8×10^{-3} p	$.90 \times 10^{-3}$ p

where p is in GeV/c.

These momentum determinations are not very good for very high momentum particles. However, the forward jet calorimeter will measure the energy of these particles to acceptable precision. Thus the critical task of the spectrometer in the forward region is to give an unambiguous determination of the sign of the particle's charge. Setting a limit for "unambiguous" of 2 standard deviations, we see that this is accomplished for particles up to 360 GeV/c with the 500 GeV/c run parameters, and over 1000 GeV/c for the 1000 GeV/c run parameters.

Appendix D

Trigger Calorimeter: Construction, Electronics, Calibration and Monitoring

The trigger calorimeter is the device used to trigger on events yielding high-p_t jets (CAL1 and CAL2 of Figure II-1) The forward calorimeter (CAL3), located downstream of the trigger calorimeter and discussed in Appendix F, will be used to measure the energy of particles in the beam jet and will not be used in the trigger.

Calorimeter

The calorimeter is divided into three sections: a front electron section consisting of lead-scintillator sandwiches, a front hadron section constructed using steel-scintillator sandwiches, and a back hadron steel-scintillator section. The front electron and hadron sections are shown as CAL1 in Figure II-1 while the back hadron section is shown as CAL2 in the same figure. Each of the three sections is constructed of many small modules, each functioning as an independent calorimeter. The modularity of the front sections, as viewed by the beam, is shown in Figure D-1. The transverse dimensions of the smaller square modules are 8" by 8". The construction of one of the modules of the front hadron section is shown in Figure D-2. The scintillator light is collected by a wavelength shifter bar (plexiglass doped with a wavelength shifter (BBQ) and an ultraviolet absorber) running along one edge of the module. The longitudinal dimensions of the calorimeter are summarized in Table D-1. Each wavelength shifter bar is read out by its own phototube. Thus the front electron section provides 158 signals referred to as E_n, n = 1 to 158. Similarly we have 158 signals from the front hadron section which we call F_n, n = 1, 158. The back hadron section provides 42 signals:

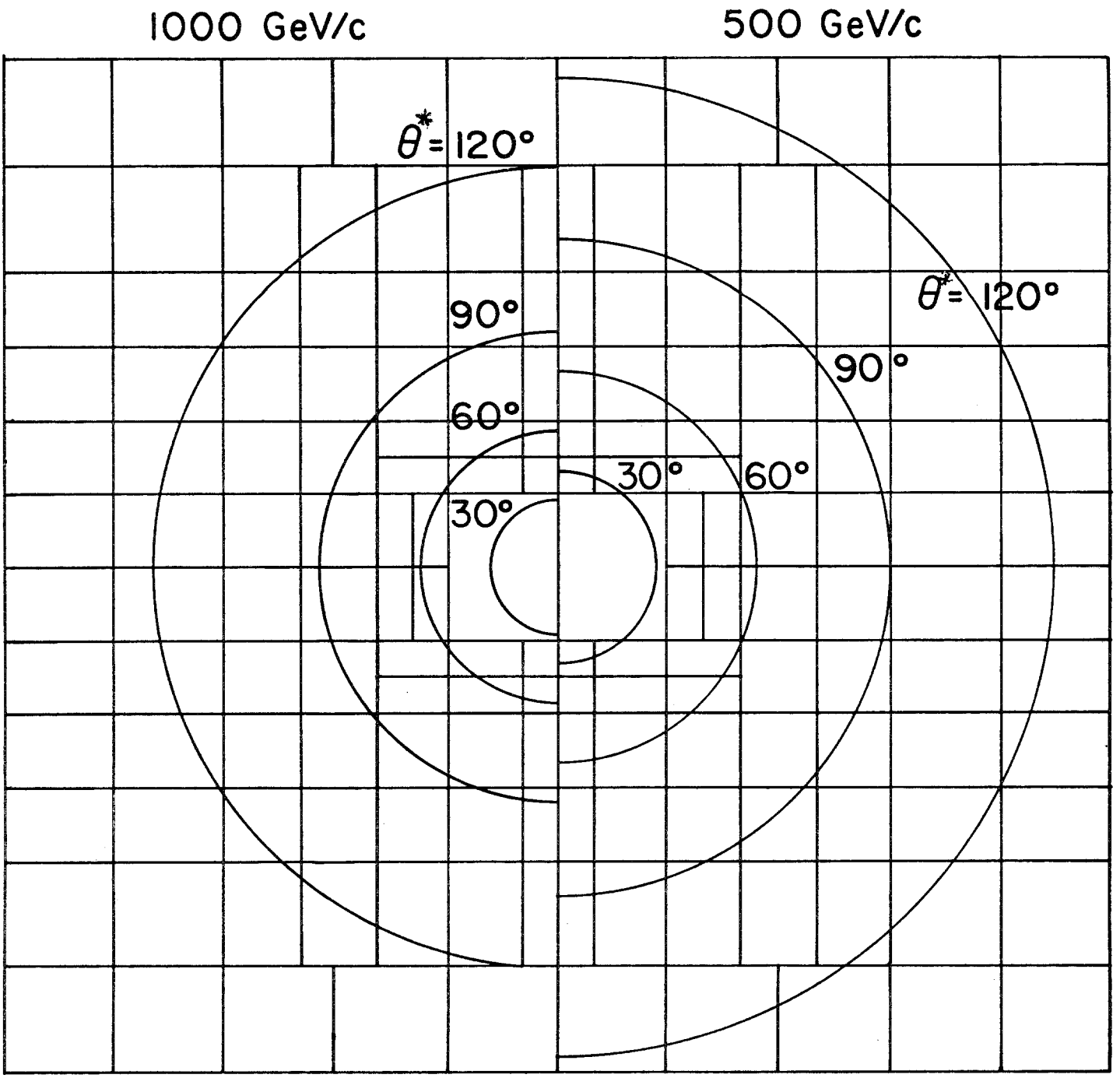

Figure D-1: Modular division of the front section of the trigger calorimeter (CAL1 of Figure II-1). The circles are circles of constant polar angle, θ^*, as measured in the hadron-hadron CMS for $\beta = 1$ particles. Two sets of circles corresponding to p_{inc} = 1000 GeV/c and 500 GeV/c are shown. The center "module" is a beam hole.

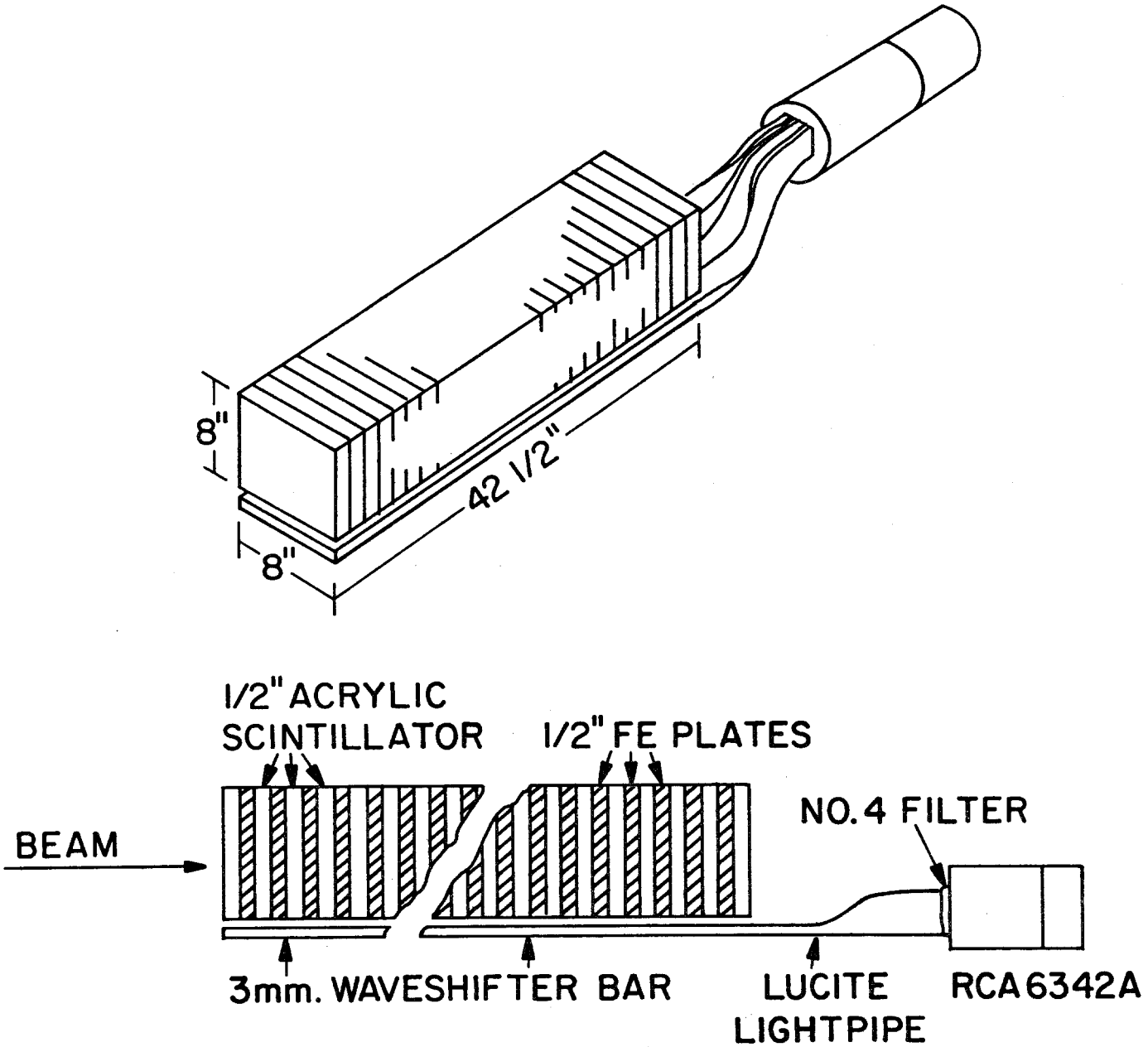

Figure D-2: Construction of a "typical" module of the trigger calorimeter. A 8" x 8" module of the front hadron section is shown.

Table D-1

Longitudinal Dimensions of the Trigger Calorimeter

Section	Material	Radiation Lengths	Absorption Lengths
Front Electron	14: 1/4" Pb	15.9	0.48
	15: 1/2" Sc	0.6	0.29
Front Hadron	40: 1/2" Fe	28.9	2.97
	40: 1/2" Sc	1.5	0.78
Back Hadron	22: 1" Fe	31.8	3.27
	22: 1/2" Sc	0.8	0.43
Total	---	79.3	8.22

B_n, n = 1,42. The segmentation of the back hadron section is shown in Figure D-3. Thus the calorimeter provides a total of 358 signals.

The calorimeter as shown in Figures D-1 and D-3 is a modified version of the calorimeter used in E557. The modification consists of adding 32 modules to each of the front sections and 14 modules to the back section. In the three sections corner modules will be added as well as a top and bottom row.

The resolution of the E557 calorimeter was measured to be $0.20/\sqrt{E(\mathrm{GeV})}$ for electrons and photons and $0.70/\sqrt{E(\mathrm{GeV})}$ for hadrons. A study of high-p_t data taken in a test run shows good uniformity.[46]

Calorimeter Acceptance

In Figure D-1 circles of constant polar angle θ^*, as measured in the hadron-hadron c.m.for $\beta = 1$ particles, are shown superimposed on the calorimeter. Two sets of circles corresponding to incident beam momenta of 500 GeV/c and 1000 GeV/c are shown. The circles show that good acceptance will be achieved over the range $60^\circ < \theta^* < 120^\circ$ for both incident momenta.

The performance of the calorimeter as a triggering device is governed by how much of the deposited energy (or transverse momentum) originated from the scattered jets. Most of the secondaries associated with the beam remnant jet go through the calorimeter hole in the vicinity of the beam line. Secondaries originating from the target remnant jet are typically at large angles. The majority of them hit the upstream face of the magnet. Consequently, it is expected that the majority of the energy deposited in the calorimeter will have originated from the scattered jets. This has been confirmed by using the Monte-Carlo simulation which shows that 85% of the deposited transverse momentum originates from the scattered jets. This fraction increases with larger transverse momentum as shown in Figure D-4.

BACK CALORIMETER SECTION

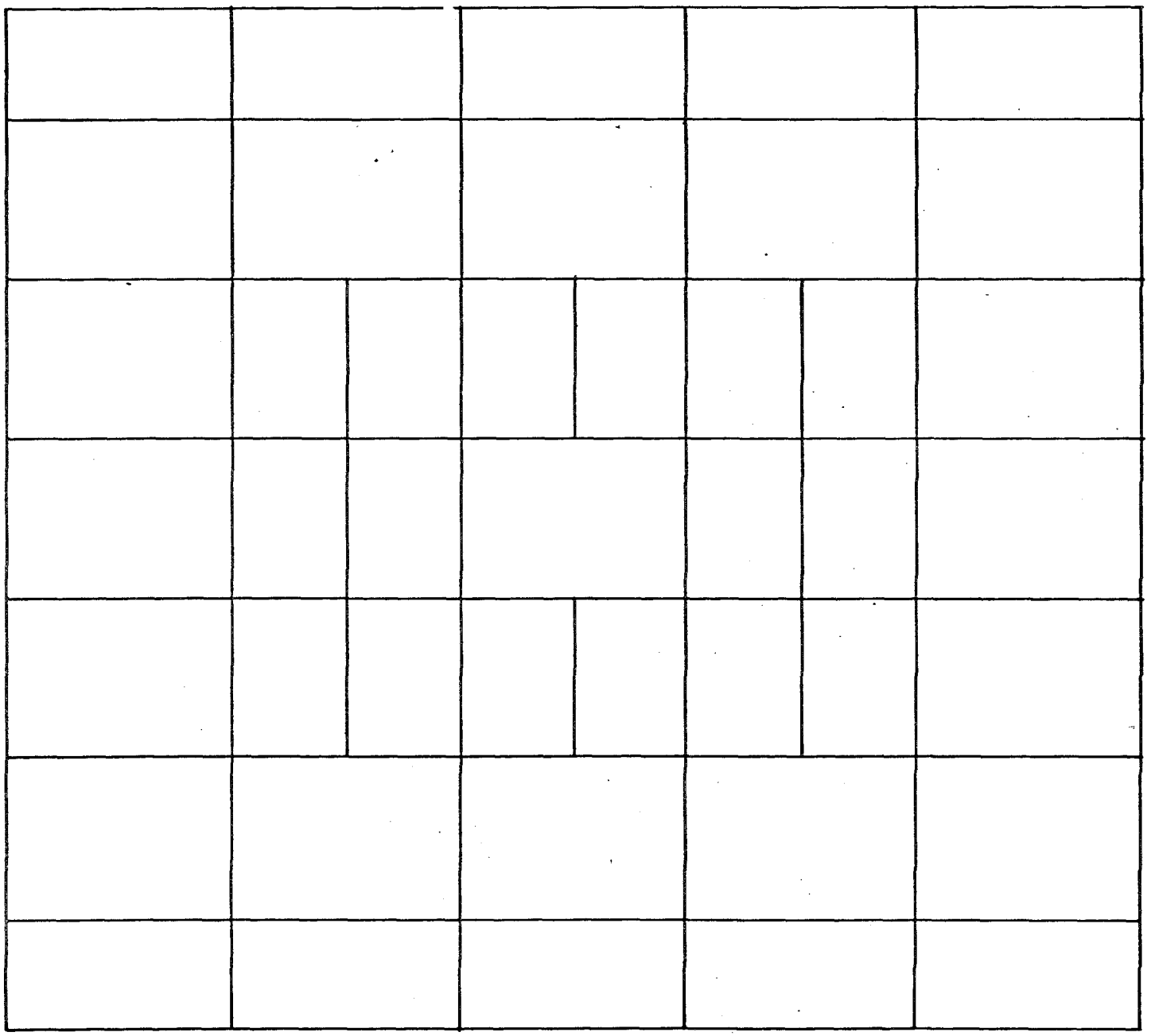

Figure D-3: Modular division of the back section of the trigger calorimeter (CAL2 of Figure II-1). The center "module" is a beam hole.

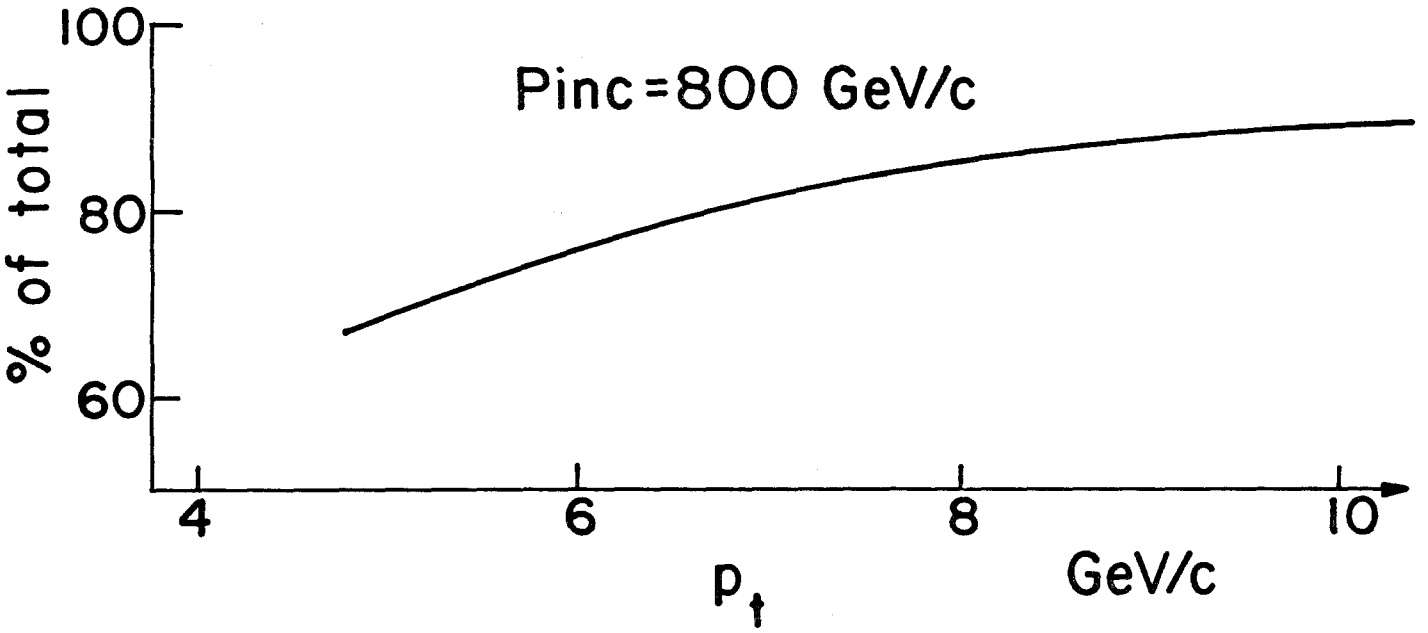

Figure D-4: Fraction of energy deposited in the trigger calorimeter contributed by the 2 scattered high-p_t jets as a function of jet p_t. This is based on a 4-jet Monte-Carlo model with p_{inc} = 800 GeV/c.

In Figure D-5 we show the acceptance of the trigger calorimeter for di-jet systems where a di-jet refers to the 2 high-p_t scattered jets. The acceptance is shown as a function of x_F, the fractional longitudinal momentum of the di-jet for $14 < M < 18$ where M is the di-jet mass and for $\Sigma|p_t| > 14$ where the sum is taken over all the particles in the di-jet. (Units are GeV.) This curve is a Monte-Carlo prediction for $p_{inc} = 800$ GeV/c.

Trigger Electronics

Each of the 358 calorimeter signals will be pulse-height analyzed and onto tape for off-line analysis. In addition these signals will be used to form the high-p_t jet trigger. As in E557 there will be several triggers which use either all of or a portion of the calorimeter. Details of how the various triggers are formed are given below.

Since we wish to trigger on p_t rather than energy the calorimeter signal from a given module must be weighted by $\sin\theta$ where θ is the angle between a line from the target to calorimeter center and a line from target to module. The p_t-weighting by appropriately adjusting the high voltage on each phototube.

The modules of the front section of the calorimeter will be divided into 16 groups as shown in Figure D-6. The grouping will be done separately for the front electron and front hadron sections. The signals of the modules in a group will be summed to yield 16 analog sum signals (SPE1 through SPE16) for the front-electron unit and 16 signals (SPF1 through SPF16) for the front-hadron unit. This summing will be accomplished using analog summing modules (First-Level-Summers) built for and used in E557. These summing modules can sum up to 10 inputs and have a fanout of 6. Subsequent summations of the outputs of the first-level-summers are performed using either Lecroy 428's or second-level-summers (electronically similar to the first-level summers but packaged in single-width NIM modules).

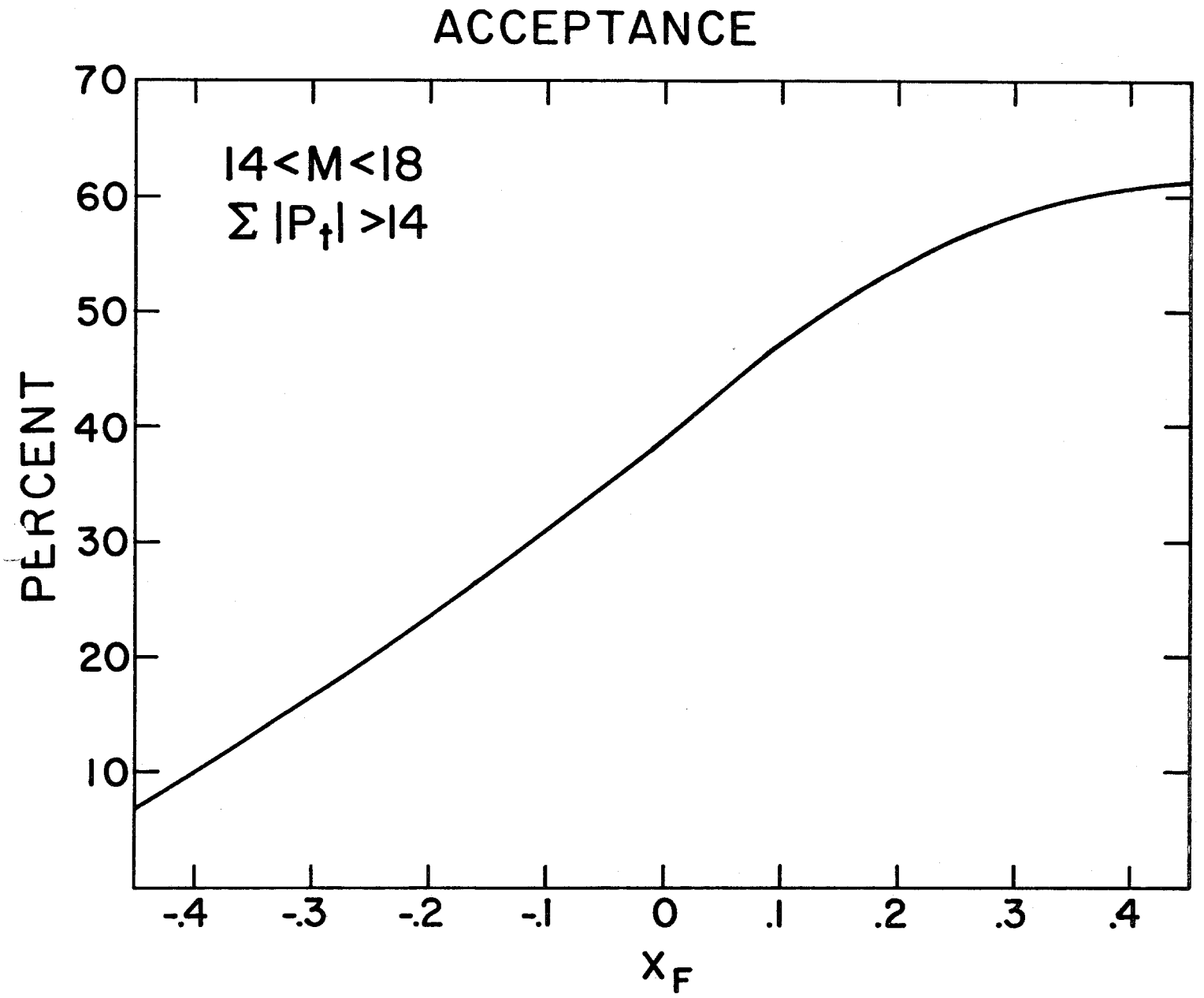

Figure D-5: Trigger calorimeter acceptance of di-jet (2 high-p_t scattered jet system) as a function of x_F (of the di-jet). M is the di-jet effective mass and $\Sigma|p_t|$ is calculated for all particles in the di-jet. This is a Monte-Carlo prediction at p_{inc} = 800 GeV/c.

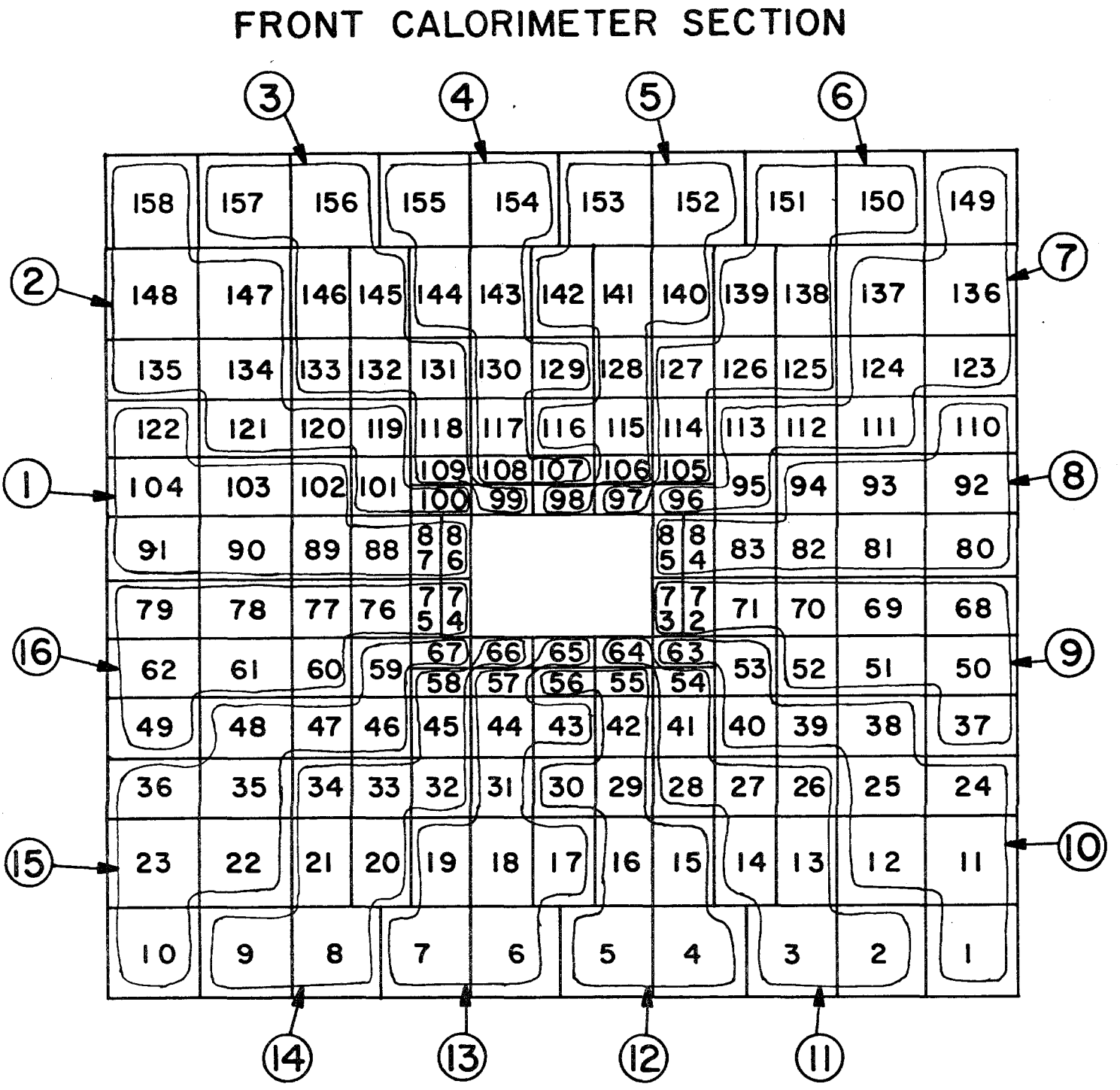

Figure D-6: Division of the front calorimeter into 16 azimuthal ϕ groups. The numbers in the modules are module numbers.

The grouping shown in Figure D-6 is such that we can more or less characterize each group by an a azimuthal angle ϕ. The first trigger formed is the "overlapped ϕ" trigger. We form the following 16 sums:

$$SPOV1 = SPE1 + SPF1 + SPE2 + SPF2 + SB$$

$$SPOV2 = SPE2 + SPF2 + SPE3 + SPF3 + SB$$

$$\vdots \qquad\qquad \vdots$$

$$SPOV16 = SPE16 + SPF1 + SPE1 + SPF16 + SB$$

where SB is the analog sum of the back-hadron section modules. We also form the following analog sums:

$$LEFT = \sum_{i=1}^{4} (SPE_i + SPF_i) + \sum_{i=13}^{16} (SPE_i + SPF_i)$$

$$RIGHT = \sum_{i=5}^{12} (SPE_i + SPF_i) + SB$$

$$TOP = \sum_{i=1}^{8} (SPE_i + SPF_i) + SB$$

$$BOTTOM = \sum_{i=9}^{16} (SPE_i + SPF_i) + SB$$

$$GLOBAL = \sum_{i=1}^{16} (SPE_i + SPF_i) + SB$$

Each of the above analog sums is input into an integrate-and-hold module which will integrate the output over about 100 ns to allow for time -jitter in signal arrival time due to wavebar, lightguide, light path and cable differences. Finally, the outputs of the integrate-and-hold are fed into discriminators. Each of the above 21 analog sums will be compared to a low (LO) and high (HI) threshold. We finally end p with

SPOVLO = OR of SPOV1 through SPOV16 (low threshold)

SPOVHI = OR of SPOV1 through SPOV16 (high threshold)

LRLO = LEFT · RIGHT (low threshold)

LRHI = LEFT · RIGHT (high threshold)

TBLO = TOP · BOTTOM (low threshold)

TBHI = TOP · BOTTOM (high threshold)

GLOBLO = (low threshold)

GLOBHI = (high threshold)

The above triggers will be run simultaneously with those triggers with higher rates scaled down so as not to saturate the overall trigger. The SPOV triggers will select events with single high-p_t particles. The LR and TB triggers will select on di-jet events while the GLOBAL trigger will simply require some minimum p_t in the calorimeter.

Monitoring System

The system used to monitor the calorimeter will be that used in E557. A UV laser will illuminate a BBQ wavelength shifted lucite sheet which will then illuminate a fiber bundle which will fan out to bulkhead connectors on a patch panel. These separate fibers will transmit the wavelength shifted light to the calorimeter. From there the light is transmitted by other fibers to the light-guide-wavebar interface and directed to the far end (away from the phototube) of the wavebar. Reflective coating at the far end of the wavebar will cause the light to be reflected back into the wavebar, across the wavebar-light guide interface and onto the phototube. Thus the phototube operation and glue joint transmission are monitored.

The outputs of the phototubes as well as the intermediate sums (second-level and integrate-and-hold) outputs will be read into ADC's which can be read by the PDP11/45 or an LSI-11. The latter will pulse the laser and monitor phototube signals and summed signals in interspill time. Thus both meter and trigger electronics will be monitored.

Calibration

Each of the modules of the calorimeter will be calibrated by moving the appropriate calorimeter module into a monoenergetic hadron and tagged electron beam. A computer-controlled, motorized calorimeter table which moves the calorimeter horizontally and vertically already exists. A special PDP11/45 version of MULTI (the online data acquisition software package) properly positions the calorimeter and adjusts the computer-controlled high-voltage of the appropriate phototubes so that the output spectra peak at some predetermined ADC channel number. The laser output is then read and recorded as a reference.

Software

Extensive diagnostic software utilizing a Tektronix terminal and a color TV display to display results of event data or laser output already exists.

Appendix E

Dimuon Trigger

In this section we describe:

1. a dimuon trigger and associated electronics; and
2. background triggers.

The Trigger

Referring to Figure II-1, the dimuon trigger that there be at least two charged particles which:

a. penetrate the trigger calorimeter (CAL1 and CAL2) and iron absorber;

b. point back to the vertex; and

c. have an effective mass greater than some minimum.

Requirement (a) requires that the particles be muons. Requirement (b) will be used to eliminate beam halo muons. Beam counters will also be used to discriminate against beam halo. A main source of background for a dimuon trigger in an "open geometry" experiment is pion decay. Dimuons arising from this source have a low effective-mass ($M\mu\mu \lesssim 3$ GeV). More details regarding this background will be given below. Thus requirement (c) is imposed. Requirement (c) is effected by requiring that both muons of a candidate pair penetrate the total length of absorber (and thus have some minimum momentum) and that the opening angle be greater than some minimum. The absorber thickness is 6600 gm/cm^2 which corresponds to a μ momentum requirement, $p > 12$ GeV/c. A typical minimum opening angle, θ_{min}, will be about 70 mr.

The hardware which imposes the above requirements consists of:

1. two PWC stations, each with an x-plane and a y-plane (μ_1 and μ_2 in Figure II-1);
2. a scintillator hodoscope (μ_3) placed downstream of the total iron absorber; and
3. a trigger processor which uses information from μ_1, μ_2 and μ_3.

The μ_1 and μ_2 PWC stations will be separated by 2.5 meters. These PWC's will have a 4-mm wire spacing with 5 wires grouped together into a single amplifier to yield 2-cm logical elements. Thus the angular accuracy of this system will be ± 4 mr. The resulting spatial resolution of the vertex expected for a 4 GeV mass dimuon pair at 1000 GeV/c incident momentum is shown in Figure E-1.

The scintillator hodoscope (μ_3) will consist of 25 vertical counters to cover the top half of the iron absorber and 25 vertical counters to cover the bottom half. Each counter will be about 2.5 meters long and 0.2 meters wide. Counters will not cover the central region through which particles in the beam jet will pass. An initial requirement will be that ≥ 2 charged particles pass through this hodoscope. Based on background studies we expect that about 100 events per 10^6 interactions will satisfy this requirement. Since we expect 10^6 interactions/second our rate for candidate triggers to be processed by further trigger logic will be about 100/second. Thus a trigger processor which can perform the calculations associated with requirements (b) and (c) in $\lesssim 1$ μsec will introduce negligible dead time in the overall experiment.

There will be approximately 200 logical elements associated with the x-plane of μ_1 (call this plane x_1); and a similar number of

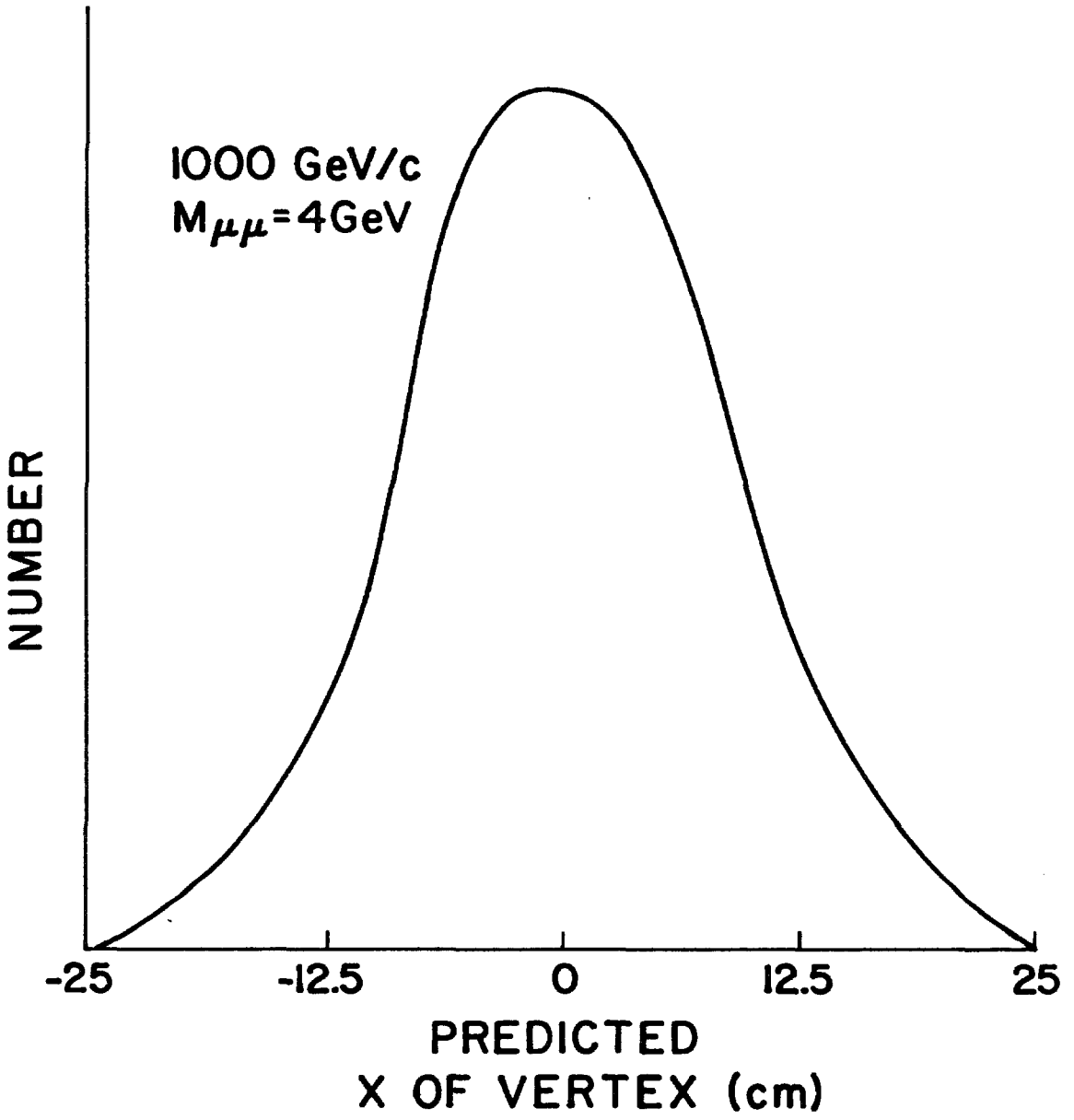

Figure E-1: Monte Carlo preduction for the vertex location of the dimuon using only measuring elements from PWC stations μ_1 and μ_2. The Monte-Carlo program assumed a dimuon mass ($M_{\mu\mu}$) of 4 GeV and p_{inc} = 1000 GeV/c.

elements associated with each of x_2, y_1 and y_2. The requirement that a track points back to the vertex implies that for a given struck x_2 element, a corresponding x_1 element should have been struck, similarly for y_2 and y_1.

A possible scheme for imposing the vertex and minimum opening angle requirements is shown schematically in Figure E-2. We first consider the x-view. The x_1 elements (we assume they number 256) are latched in a register while the x_2 elements are stored in a shift register. The outputs of these registers are ANDed together pairwise (a x_2 element and the corresponding x_1 element pointing to the vertex). The OR of the AND outputs determines whether at least one match was found.

The x_2 shift register is then shifted 1 bit right and 1 bit left to see if a match is found. This allows for jitter in the hit pattern. This shifting process can be repeated up to N times (specified by a computer loaded control word). If a match is found the outputs of the AND gates are latched in a register ($\mathbf{x}_v$ in Figure E-2) and then passed on to two priority encoders which encode x_{min} and x_{max}. The difference of x_{max} and x_{min} is computed and squared. Thus the result is $(\Delta x)^2$ where

$$(\Delta x)^2 = (x_{max} - x_{min})^2$$

If there are only two tracks which point back to the vertex then $|\Delta x|$ is their separation in the x-view. If there are more than 2 tracks then $|\Delta x|$ is the maximum separation. Similar electronics will find $(\Delta y)^2$. The condition that at least one pair of tracks has a minimum opening angle will be equivalent to requiring:

$$(\Delta x)^2 + (\Delta y)^2 > c^2$$

where c is adjustable.

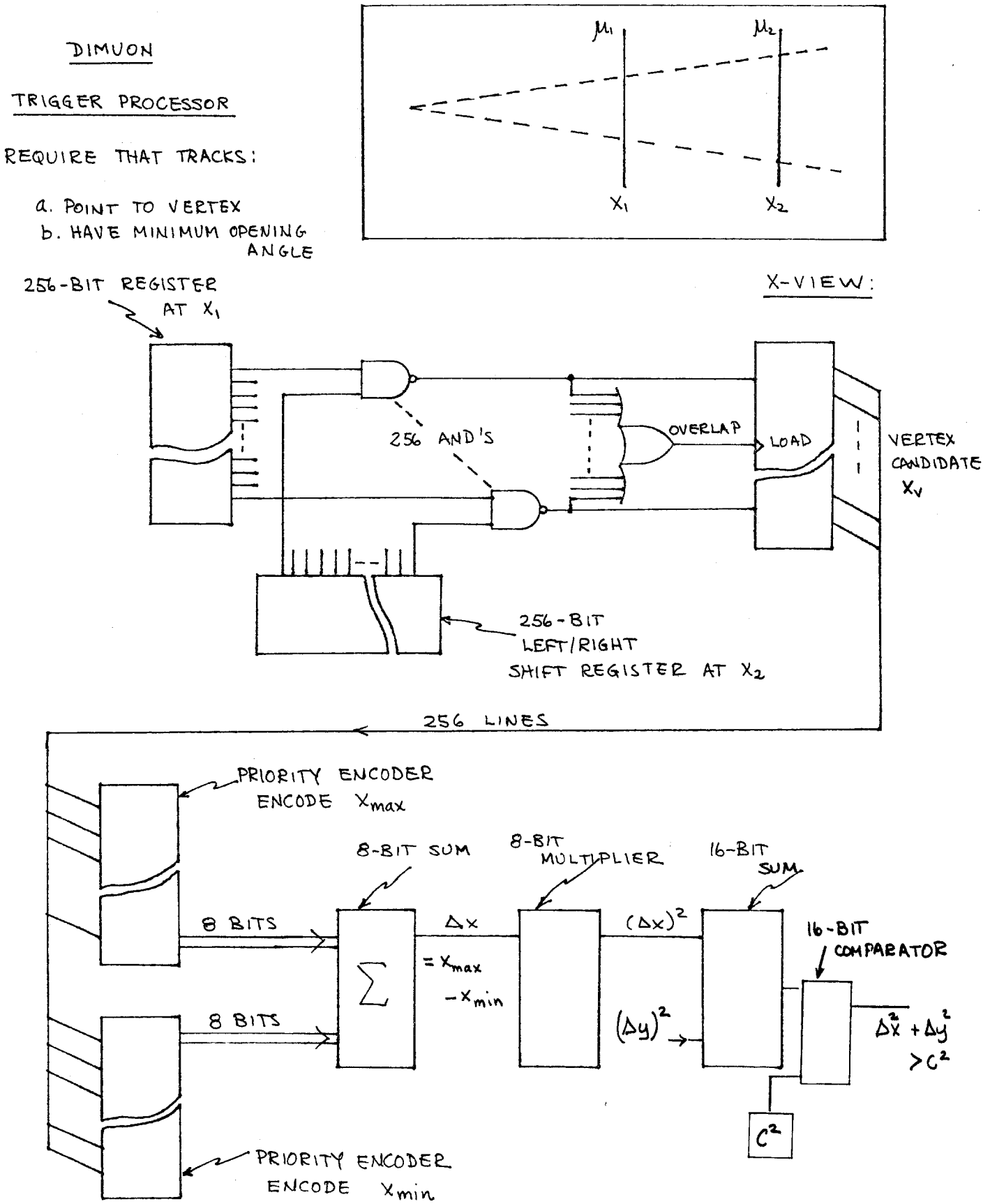

Figure E-2: Schematic of a possible dimuon trigger processor to require that tracks point to vertex and have a minimum opening angle.

Finally, we will count the number of muon candidates to anticipate situations where a large number of hits in plane μ_2 would have a large probability of satisfying the θ_{min} and vertex requirements. We will have the option of rejecting triggers when μ_2 has too many hits.

The processor described above should be able to perform the logic in about 1 to 2 μsec.

Background and Acceptance

The background from π decay was estimated in the following manner. The multiplicity of charged pions was assumed to be that measured in Fermilab bubble chamber experiments.[47] Each pion was then given an x and p_t according to inclusive distributions in these variables reported in the same reference. No attempt was made to conserve energy or momentum. No particle correlations were made.

The lower curves in figure E-3 shows the resulting background trigger rate due to these μ's at 500 GeV/c. A θ_{min} of 70 mr, for example, would give 1 trigger per 10^6 interactions. The same figure shows the yield of real (prompt) dimuons as a function of θ_{min} for a dimuon mass of 6 GeV. The upper curves of Figure E-3 show the acceptance as a function of dimuon mass for θ_{min} = 70 mr at the two beam momenta. We are continuing these background studies but feel that the background rates quoted above are correct to within an order of magnitude. Our trigger rate prediction (see page V-1) corresponds to 6 triggers/10^6 interactions.

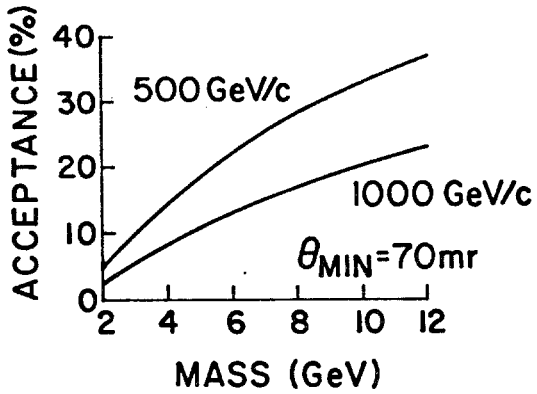

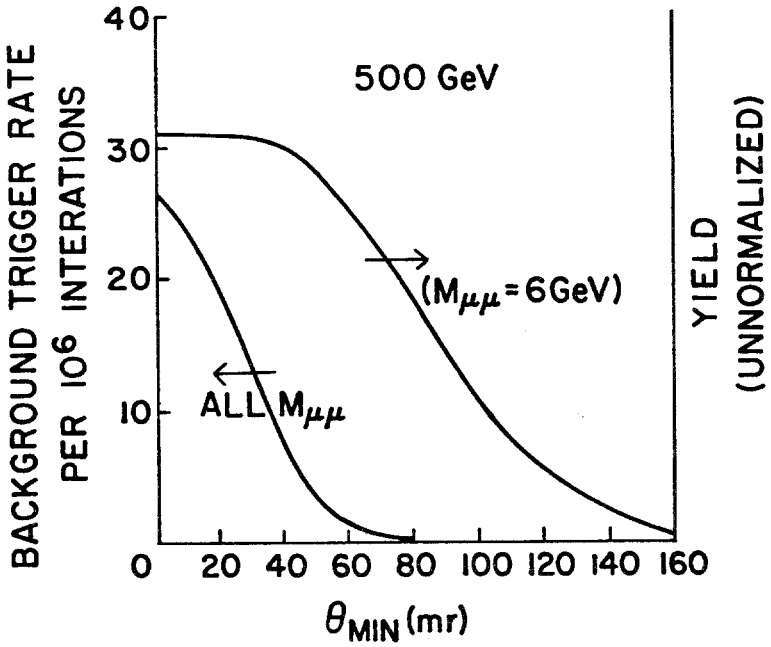

Figure E-3:

(a) Dimuon acceptance as a function of dimuon mass for p_{inc} = 500 GeV/c and 1000 GeV/c assuming a minimum opening angle (for the dimuon) of equal to 70 mr.

(b) Background dimuon trigger rate due to π decays as a function of θ_{min} (the dimuon minimum opening angle). Also shown is the unnormalized yield for prompt dimuons (mass = 6 GeV) for p_{inc} = 500 GeV/c.

Appendix F

Forward Calorimeter

We discuss here the calorimeter at the far downstream end of the experiment consisting of an electromagnetic calorimeter with 144 segments and a hadronic calorimeter of 96 segments. The calorimeter is the main instrument used to analyze the forward jet.

The calorimeter dimensions, determined by the size of the hole in the existing calorimeter, and the need to separate close together particles in the forward jet, are 54" high by 80" wide overall (1.37m by 2.03m). The segmentation has been determined by Monte Carlo simulation of the forward jet in $\mu^+\mu^-$ triggers to bring the probability of two particles into one calorimeter segment down to acceptable levels. The beam jet in dimuon events tends to be more collimated than the beam jet produced in association with high-p_t jets. The resulting layout is shown in Fig. F-1, a view of the calorimeter looking downstream.

The calorimeter we describe below is of a conservative design; its workability has been demonstrated in E557 testing. There are, however, several possible new design approaches which may lead to improved performance. We intend to study these options. One possibility arises from the shrinkage of the lateral distribution of hadron showers with increasing energy. For example, for a 100 GeV proton incident on iron, 50% of the particles are within a radius of 1 cm at a depth of 336[48] gm/cm^2 (about 3 interaction lengths) Because the lateral distribution is so sharply peaked, multiple incident hadrons with overlapping cascades may be separated if there is sufficient spatial resolution in the sampling detectors. For

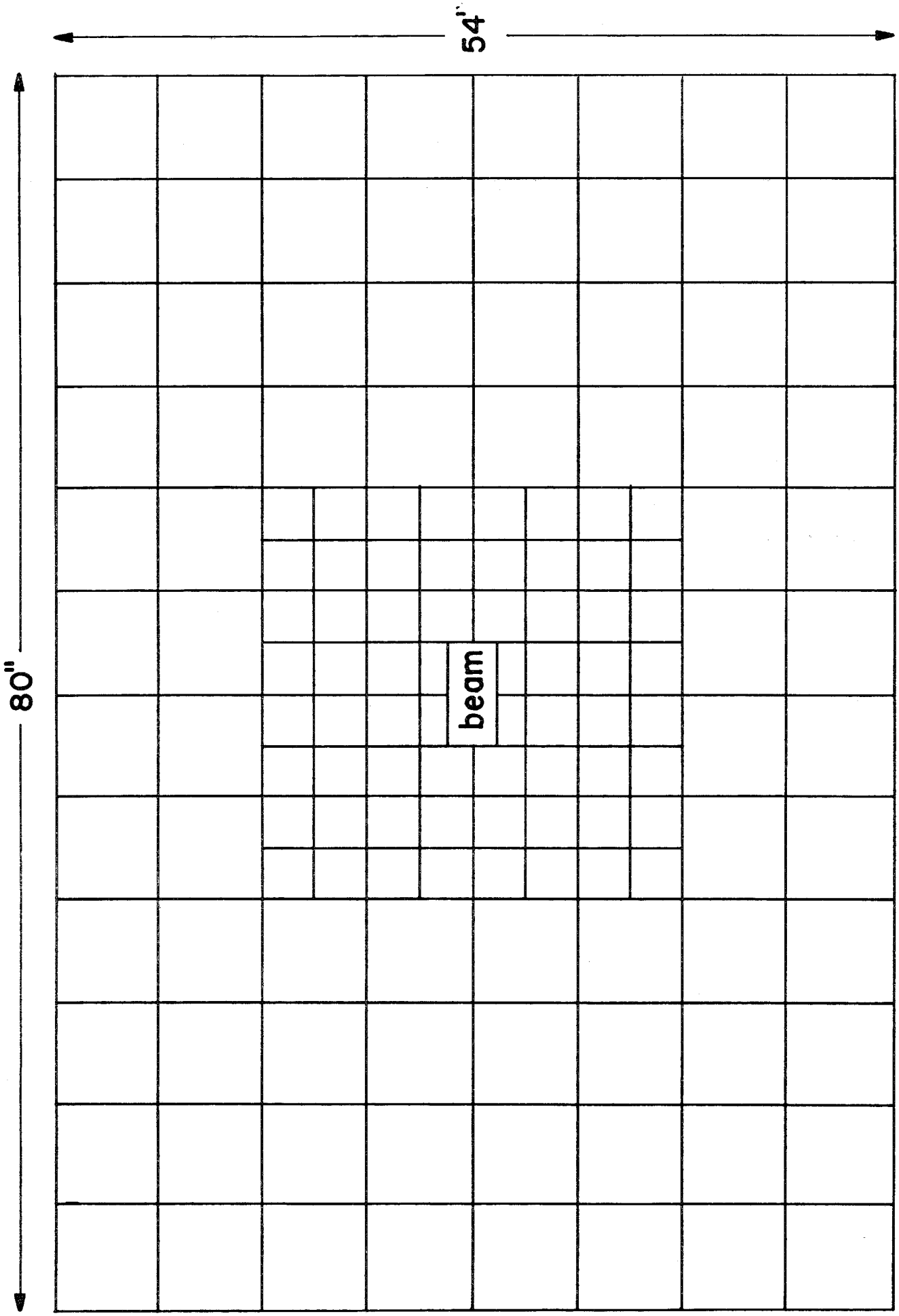

Figure F-1: Segmentation of the forward calorimeter (CAL3 in Figure II-1).

this reason, we will study the possible use of PWC's in the proportional mode rather than scintillators. These have already been successfully used by Aubert et al.[49] in an electromagnetic calorimeter.

A Forward Calorimeter Design Based on the E557 Calorimeter

The calorimeter is constructed of 24 "trays" each 27" wide, 6 3/4" high and 106" deep along the beam direction, containing an electromagnetic section of eighteen 1/4" lead sheets followed by sixty 1" steel sheets interspersed with 1/2" "Altustipe" acrylic based scintillator pieces. These pieces are 6 1/2" x 6 1/2" around the outside and 3 1/4" x 3 1/4" in the central 32" x 32" region in the electromagnetic section where the particle density is higher. The hadronic section has 6 1/2" x 6 1/2" pieces throughout. The probability of two particles into an electromagnetic segment is at worst 12% of the single particle probability with 1000 GeV/c incident beam. This confusion is four times worse in the hadronic sections in the center region only if we count all particles; counting only hadrons (about 50% of the total) there is less confusion. Of course, the situation is much better at 500 GeV/c. The above discussion shows why the calorimeter must be so far downstream and so large.

The readout is by wavebars in a manner similar to the present E557 calorimeter. The electromagnetic section light comes out in an upstream direction. It then follows light pipes to photomultipliers above and below the calorimeter. The wavebars for the hadronic section, coming out the rear, are quite long (90") but our measured attenuation length of 12 meters (E557 wavebars) allows compensation by masking. We may read each hadronic section with 2 photomultipliers giving better lateral resolution. In the 3 1/4" x 3 1/4" region additional wavebars are inserted in central slots in the electromagnetic calorimeter. The wavebars are put on the side away from the beam, which

passes through a 4" high by 6 1/2" wide hole. This hole, barely large enough to clear the beam size 43 meters downstream of the target and to accommodate analysis magnet reversals, must be kept as small as possible. These dimensions result in the loss of a jet fragment in about 1/3 of the events at 1000 GeV/c.

Monitoring of gains between calibrations is to be done using μ's between events.

We have discussed segmentation; the resolution of this calorimeter will be about as good as that measured in E557 i.e. $\sigma = 0.7/\sqrt{E(\mathrm{GeV})}$ hadronic and better than $0.2/\sqrt{E}$ electromagnetic.

Appendix G

Chamber System for Particle Tracking

The system of proportional and drift chambers to be used for determining charged particle trajectories is summarized in Table G-1. In this table we indicate which items already exist for E557, which items are planned in the near future for current experiments and which items must be added for the proposed experiment.

The beam chamber system (BA, BB) will approach space charge saturation at an incident beam flux of $.5 \times 10^6$/sec. To overcome such rate limits we wish to consider improvements such as a multistep chamber[50] or a scintillator hodoscope. Although event vertices are generally reconstructed without beam information, such information is useful in eliminating the overlapping event background discussed earlier in Section III.

The cylindrical proportional chamber β is to be used for determining the azimuth and multiplicity of large angle tracks. The A station will be used as is We expect some inefficiency due to multiple hits on one wire (especially for events originating at the downstream end of the target) and some saturation in the beam area. The vertex reconstruction relies mainly on the largest angle tracks, which are least affected by these problems. The B and C stations are as used in several experiments; C is far enough into the magnet fringe field that deflections of charged particles are generally negligible.

Station D, just after the magnet, will be supplemented by a 320-wire 1 mm wire spacing PWC (D´) covering the beam region in order to improve the momentum

Table G-1

Chamber System

Station	Wire Spacing (mm)	Planes Number: Orientation	Type	Number of Wires	Transverse Dimensions (m)	Status
BA, BB	2	2:x, 2:y, 1:u(45°)	PWC	280	0.11 x 0.11	Exists
BB	1	1:x, 1:y, 1:u(45°)	PWC	96	0.03 x 0.03	Exist
β	2	1: cylindrical covering 2π azimuth	PWC	192	0.085 (radius)	Exist
A	1	2:x, 2:y, 1:u(45°), 1:v(-45°)	PWC	1536	0.26 x 0.26	Exist
B	2	3:x, 1:y, 1.u (45°)	PWC	2368	0.64 x 1.02	Exist
C	2	1:x, 1:y	PWC	832	0.64 x 1.02	Exist
D	2 3(for y)	2:x, 2:y, 1:u(-15°), 1:v(15°)	PWC	4416	1.00 x 1.61 to 1.14 x 1.94	Exist 2:y being built
D'	1	x	PWC	320	0.32 x 0.22	New
E	19	8:x, 4:u(15°),4:v(-15°)	Drift	3200	1.68 x 3.05	$\frac{1}{2}$ being built $\frac{1}{2}$ new
E'	2	2:x, 1:y, 1:u(45°), 1:v(-45°)	PWC	1600	0.64 x 0.64	Exist 1:x New
F	2	2:x, 1:y, 1:u(45°), 1:v(-45°)	PWC	1856	0.90 x 0.90	New
G	4.6	2:x, 2:y	PWC	1280	1.48 x 1.48 (staggered)	Exist

resolution on the fastest tracks as discussed in Appendix C. This will be constructed in such a way as not to introduce appreciable scattering material in the spectrometer aperture. The new 3 mm Dy chambers will have been built for the second E557 run and for E623.

The drift chamber system currently under construction for the MPS has a vertical aperture (168 cm), which is less than the E557 calorimeter (223 cm), let alone the vertically expanded calorimeter needed for this proposed experiment (279 cm). The vertical limit was dictated both by existing construction facilities and the sharply escalating difficulties generally encountered in larger chambers. Thus the two modules (each x, u, v, x') will have to be staggered vertically to cover the calorimeter. This generates two problems: frame material in front of the calorimeter (which we feel is acceptable) and an overlap of only 57 cm. The latter problem means that 222 cm. of the vertical aperture is covered by only one xuvx' set which is insufficient for forming tracks in high multiplicity events. In order to overcome this pattern recognition problem we will need an additional set of modules identical to those currently being constructed. Our Monte Carlo studies indicate that the wire spacing (19 mm; 9.5 mm maximum drift) of the drift chambers is small enough to handle the expected multiplicities despite readout of only one hit per wire. Particle positions in the central region will also be measured by 64 cm x 64 cm PWCs (E').

Station F, consisting of five 2 mm PWCs, is intended to improve track finding of the close-together forward going particles. These tracks will be confirmed by a set of PWCs (Station G) just before the forward calorimeter. These 4.6 mm wire spacing chambers now exist, having been used in E260 and now in storage. Since each has a 148 cm. x 148 cm. aperture, they will have

to be staggered horizontally to cover the 137 cm. x 203 cm. calorimeter. Thus the central region will have two x and two y coordinate measurements.

The total number of PWC wires will be 14,816; the present count is 10,336. Thus we need 4480 additional channels (current electronics and cabling cost about $15/channel). The drift chamber readout system must be doubled from 1600 to 3200 channels. These numbers do not include any improvements to the target region beyond the existing β chamber.

Appendix H

Monte Carlo Simulation

In this appendix we discuss the Monte Carlo of Dimuon and High-p_t Jet Triggers.

1. Monte Carlo Simulation of the Drell-Yan Process (Dimuon Triggers)[51]

In order to simulate events described by the diagram of Figure H-1, we follow the procedure outlined below:

(a) h_1 is chosen to be either a π^+ or π^- and h_2 to be a proton;

(b) The annihilating quarks Q_1 and Q_2 are chosen as either sea or valence quarks according to a prescription outlined below. So $Q_1 = Q$ and $Q_2 = \bar{Q}$.

(c) The quark initiating the beam jet (Q_B) is correlated with Q_1. In some cases the forward going system will consist of a leading hadron h_ℓ where $h_\ell = h_1$ along with Q_B which fragments into the beam jet.

(d) The quark initiating the target jet (Q_T) is chosen to be a u quark. For acceptance studies the important jet for our purposes is the beam jet. The target jet provides a background of low momentum particles and the details of the quark initiating this jet are not important for our studies. The fractional longitudinal momentum of Q_T is $1-x_2$.

(e) For a given momentum, p_{beam}, the dimuon mass (M) along with the Feynman x (x_F) and transverse momentum (p_t) of the dimuon pair are chosen to follow the measured distributions in the variables as reported by Barate *et al.*[27]

(f) The fractional longitudinal momenta for Q_1 and Q_2 (x_1 and x_2 respectively) are determined from s ($\cong \sqrt{2M_p p_{beam}}$), M and x_F

$$x_1 - x_2 = x_F$$

$$x_1 \cdot x_2 = \frac{M^2}{s}$$

(g) The assumption is that Q_1 (Q_2) with x_1 (x_2) less than 0.1 are "sea" quarks whereas Q_1 (Q_2) with x_1 (x_2) greater than 0.1 are valence quarks. We consider the possible forward going system for the four regions of x_1, x_2 in Table H-1.

Table H-1

x_1	x_2	Forward-going system
<0.1	<0.1	h_ℓ plus $Q_B \rightarrow$ jet
<0.1	>0.1	h_ℓ plus $Q_B \rightarrow$ jet
>0.1	<0.1	$Q_B \rightarrow$ jet
>0.1	>0.1	$Q_B \rightarrow$ jet

Notice that the forward going system includes a leading hadron ($h_\ell = h_1$) when $x_1 < 0.1$. Since in this case the valence quarks of h_1 are not annihilated we assume that the leading particle comes off intact with reduced momentum. In fact the fractional momentum of h_ℓ is chosen to be $y(1 - x_1)$ where y is uniformly distributed between 0 and 1. The fractional momentum of the accompanying Q_B is then $(1 - y)(1 - x_1)$.

(h) The flavor of Q_B is chosen according to the following assumptions.

(1) If Q_1 is picked from the "sea", quark and antiquark appear with equal likelihood with the probabilities of finding u, d, s taken as 0.45, 0.45 and 0.10 respectively.

(2) The probability of quark annihilation will be weighted by the quark charge.

So we have: Q_B probabilies as indicated in Table H-2.

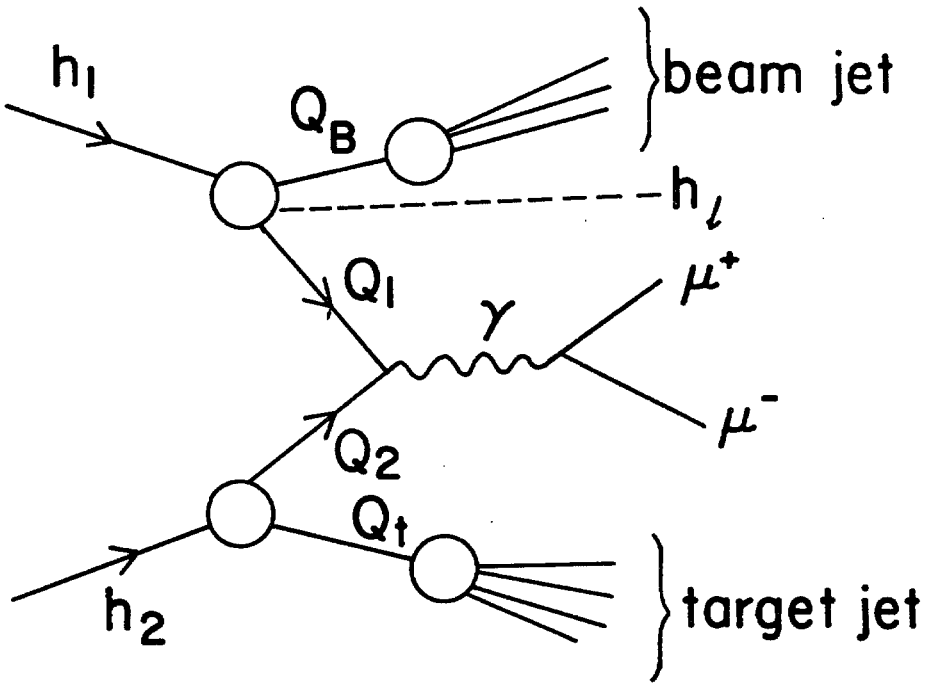

Figure H-1: Diagram assumed for dimuon production.

Table H-2

$h_1 = \pi^-$

x_1	x_1	h_ℓ	Probabilities					
			u	$\bar{u}$	d	$\bar{d}$	s	$\bar{s}$
<0.1	<0.1	π^-	.38	.38	.10	.10	.02	.02
<0.1	>0.1	π^-	.89	0.	.11	0.	0.	0.
>0.1	<0.1	-	0.	.20	.80	0.	0.	0.
>0.1	>0.1	-	0.	0.	1.0	0.	0.	0.

$h_2 = \pi^+$

x_1	x_2	h_ℓ	Probabilities					
			u	$\bar{u}$	d	$\bar{d}$	s	$\bar{s}$
<0.1	<0.1	π^+	.38	.38	.10	.10	.02	.02
<0.1	>0.1	π^+	.89	0.	.11	0.	0.	0.
>0.1	<0.1	-	.20	0.	0.	.80	0.	0.
>0.1	>0.1	-	1.0	0.	0.	0.	0.	0.

(j) Q_B and Q_T equally share the p_t required to balance the p_t of the dimuon.

(k) The LUND jetmaker (Ref: "A Monte Carlo Program for Quark and Gluon Jet Generation: by Sjostrand, University of Lund preprint LU TP 80-3) is used to fragment Q_B and Q_T.

(l) The muons are emitted isotropically in the dimuon rest frame.

Results:

The fraction of events in various x_1, x_2 regions for 500 GeV/c and 1000 GeV/c are given in Table H-3:

Table H-3

p_{beam} = 500 GeV/c

x_1	x_2	Quark Types	% of Events
<.1	<.1	Sea-Sea	0%
<.1	>.1	Sea-Valence	17%
>.1	<.1	Valence-Sea	68%
>.1	>.1	Valence-Valence	15%

p_{beam} = 1000 GeV/c

x_1	x_2	Quark Types	% of Events
<.1	<.1	Sea-Sea	4%
<.1	>.1	Sea-Valence	20%
>.1	<.1	Valence-Sea	73%
>.1	>.1	Valence-Valence	3%

Monte Carlo Simulation of the High-p_t Jet Production

The simulation of jets falls into three main stages:

1) Choosing the original partons and their momenta.

2) Scattering the partons.

3) Fragmenting the partons.

In detail:

1) Partons within the hadron were chosen according to the structure functions given in Ref. 16 . The momenta of the partons were chosen using the same structure functions. Only momenta large enough to produce a transverse momentum above a minimum value were used. This avoided generating a large number of low p_t events.

2) The partons were then scattered according to the 1st order QCD amplitudes

3) The partons were fragmented according to the Lund group's scheme. Gluons were fragmented assuming that they coupled to a $q\bar{q}$ pair. Diquarks were fragmented in the same manner as u quarks.

No scale breaking effects were included in the structure functions or the fragmentation functions. Hard gluon bremsstrahlung was not included in the program. Consequently, the 3-jet structure seen at PETRA was not apparent in our simulated events.

References

1. S. D. Drell and T. M. Yan, Phys. Rev. Lett. 25, 316 (1970)
2. E. L. Berger, Invited paper published in the Proceedings of the 3rd International Conference at Vanderbilt University on New Results in High Energy Physics, March 6-8, 1978.
3. R. P. Feynman, R. D. Field and G. C. Fox, Phys. Rev. D18, 3320 (1978)
4. M. Jacob and P. V. Landshoff, Phys. Reports 48, 285 (1978)
5. C. Bromberg et al., Phys. Rev. Lett. 38, 1447 (1977)
6. C. Bromberg et al., Nucl. Phys. B134, 189 (1978)
7. C. Bromberg et al., Phys. Rev. Lett. 42, 1202 (1979)
8. C. Bromberg et al., Phys. Rev. Lett. 43, 561 (1979)
9. C. Bromberg et al., Phys. Rev. Lett. 43, 565 (1979)
10. C. Bromberg et al., Phys. Rev. Lett. 45, 769 (1980)
11. C. Bromberg et al., Nucl. Phys. B171, 1 (1980)
12. C. Bromberg et al., Nucl. Phys. B171, 38 (1980)
13. M. D. Corcoran et al., Phys. Rev. Lett. 41, 9 (1978)
14. R. Hogan and M. Jacob, CERN Preprint: TH2824-CERN.
15. J. F. Owens, E. Reya and M. Gluck, Phys. Rev., D18, 1501 (1978)
16. R. Field and R. Feynman, Nucl. Phys. B136, 1 (1978)
17. G. Wolf, DESY Preprint: DESY, DESY 80/85.
18. W. Furmanski and S. Pokorski, Nucl. Phys. B165, 365 (1980)
19. M. J. Teper, Phys. Lett. 90B, 443 (1980)
20. K. Konishi, A. Ukawa and A. Veneziano, Nucl. Phys. B157, 45 (1979)
21. C. Petersen and T. Walsh, Phys. Lett. 91B, 455 (1980)
22. We define $z = |p|/|p_{JET}|$ where p is the momentum of a particle in the jet. Thus $0 < z < 1$.
23. Each particle in the jet carries a momentum fraction, z, of the jet. z_1 and z_2 are the momentum fractions of the fastest and second fastest particles in the jet respectively.

24. See review by G. Matthiae, CERN-EP/80-183, to be published in the Revista del Nuovo Cimento.

25. J. K. Yoh et al., Phys. Rev. Lett. 41, 684 (1978)

26. K. J. Anderson et al., Phys. Rev. Lett. 42, 944 (1979)

27. R. Barate et al., Phys. Rev. Lett. 43, 1541 (1979)

28. E. L. Berger, Invited Review Presented at the XV Recontre de Moriond, Les Arcs, Franch, March, 1980.

29. L. Lyons, Oxford Preprint to be published in Progress in Particle and Nuclear Physics.

30. M. J. Corden et al., Phys. Lett. 68B, 96 (1977)

31. D. Drijard et al., Nucl. Phys. B156, 309 (1978)

32. A. Kernan, Bull. Am. Phys. Soc. 25, 4, April, 1980 Session BB2

33. T. A. DeGrand and H. I. Miettinen, Phys. Rev. Lett. 40, 612 (1978)

34. Actually both valence and sea quarks are involved in the annihilation process. The relative importance of each type depends on the fractional momentum carried by the annihilating quarks which is determined by the fractional momentum and mass of the dimuon system. See Appendix H for more details.

35. D. Garbutt et al., Phys. Rev. Lett. 67B, 355 (1977), L. Kluberg et al., Phys. Lett. 38, 670 (1977)

36. J. H. Kuhn, Phys. Rev. D13, 2948 (1976)

37. A. Krzywicki Phys. Rev. D14, 152 (1976)

38. G. C. Fox and S. Wolfram, Nucl. Phys. B168, 285 (1980)

39. For a general discussion of the MPS facility see A. Dzierba, E. Malamud and D. McLeod, report prepared by the Multiparticle Spectrometer Workshop, Fermilab, 1977 (unpublished); E. Malamud, unpublished notes of Lecture 5 in Fermilab Academic Lectures Series, 1976; Proposals E557, E580, E623.

40. Flux curves from Tevatron II design report.

41. Calculation by D. Carey. Private communication.

42. R. Glasser, Tevatron Workshop (Summer, 1980)

43. As summarized by K. Pretzel, preprint of a report presented at the Madison Conference (July 17-23, 1980)

44. L. Myrianthopoulos et al., University of Maryland preprint ORO 2504-320 (1980)

45. Charpak et al., CERN EP/80-179, 30 Sept. 1980 and references therein.

46. P. Rapp et al., E557 Group preprint (to be submitted for publication).

47. J. Whitmore, Physics Reports, 27, 188 (1976)

48. Monte Carlo Calculations by W. V. Jones, Proc. 11th International Cosmic Ray Conference, Budapest (1970), V4, p. 513.

49. B. Aubert et al., Proc. Wire Chamber Conference, Vienna (1980) (LAPP pre-print LAPP-EXP-03)

50. Breskin et al., Nucl. Inst. and Methods 161, 19 (1979)

51. We wish to thank F. Paige for his help in outlining this procedure.